Astronomy & Astrophysics manuscript no. aa60647-26
July 20, 2026
©ESO 2026

arXiv:2607.15355v1 [astro-ph.EP] 16 Jul 2026

Very Large Telescope observations of interstellar comet 3I/ATLAS

III: High-resolution monitoring of CN and forbidden oxygen emission across the perihelion passage with ESPRESSO

Baltasar Luco[1]⋆, Thomas H. Puzia[1], Rohan Rahatgaonkar[1], Juan Pablo Carvajal[1], and Prasanta K. Nayak[1]

Institute of Astrophysics, Pontificia Universidad Católica de Chile, Av. Vicuña Mackenna 4860, 7820436 Macul, Santiago, Chile

Received 29 April 2026 / Accepted 14 July 2026

ABSTRACT

Context. 3I/ATLAS is only the third known interstellar object to traverse the Solar System, and the first for which both branches of the perihelion passage can be monitored at high spectral resolution.
Aims. We aim to characterize in 3I/ATLAS the heliocentric evolution of the CN production rate and the forbidden [O I] emission; to describe the broader emission-line inventory; and to release the analysis tools and reduced data products to the community.
Methods. We obtained high-resolution ($R \simeq 140\,000$) spectroscopy of 3I/ATLAS on 23 nights with VLT/ESPRESSO ($r_h = 1.67 - 2.45$ au). CN production rates were derived by fitting the $B^2\Sigma^+ - X^2\Sigma^+$ band, using CometSpec, a publicly released Python package for flexible fluorescence modeling. The three forbidden [O I] lines were modeled to derive the green-to-red (G/R) flux ratio and a CO_2/H_2O proxy. Both quantities were fitted with both symmetric and piecewise-asymmetric power laws.
Results. We detect CN on 18 of 22 useful nights. We fit $Q_{CN} = a\,(r_h/1\ \mathrm{au})^b$ to the production rate versus heliocentric distance relation. The pre-perihelion CN power-law index is $b_{pre} = -4.62^{+1.25}_{-1.22}$, within the range observed for solar-system comets. The CN residuals about the smooth model show substantial scatter that we attribute to a combination of systematics and possible physical drivers that the present cadence cannot disentangle. The G/R ratio decreases from $\sim 0.42 \pm 0.14$ at $r_h \simeq 2.4$ au to $\sim 0.114 \pm 0.004$ near perihelion. The asymmetric piecewise oxygen fit is strongly preferred over the symmetric one, consistent with thermal-inertia models, although denser post-perihelion sampling would be needed to confirm this. The CO_2/H_2O proxy spans ~ 0.06–1.06 and is comparable to the values reported by Subaru/HDS and SPHEREx, and to those measured for 2I/Borisov. We additionally identify Ni I and Fe I, and report post-perihelion production rates for C_2 and CH.
Conclusions. Our high-resolution monitoring of 3I/ATLAS reveals a CO_2-rich coma that becomes progressively H_2O-dominated near perihelion, with a G/R asymmetry consistent with delayed H_2O sublimation predicted by thermal-inertia models. Together with the public release of CometSpec and the reduced data, these results provide both an empirical reference and a methodological framework for the next generation of interstellar-object monitoring campaigns.

Key words. comets: general – comets: individual: 3I/ATLAS – interplanetary medium – protoplanetary disks

1. Introduction

Comets offer a unique window into the chemistry of cosmic ices and the radiative and collisional processes operating in tenuous gas. As a comet approaches the Sun, the differential sublimation of parent compound, and their subsequent photodissociation, defines the chemical pathways traced by the species we observe in the coma. Comprehensive monitoring of different comet types is the foundation for building a self-consistent and complete dataset that enables a thorough study of their chemistry and morphology. In this work, we focus on two complementary diagnostics accessible to high-resolution optical spectroscopy: the CN violet band and the forbidden [O I] lines.

The CN $B^2\Sigma^+$–$X^2\Sigma^+$ violet band is one of the most prominent features in cometary spectra and was among the first molecules detected in comets, remaining detectable beyond $r_h \simeq 3$ au owing to its high fluorescence efficiency. CN is produced primarily by photodissociation of HCN (Combi & Delsemme 1980), although in some cases additional production channels must be invoked to explain the observed CN abundance (e.g., Fray et al. 2005). At sufficient spectral resolution and signal-to-noise ratio, the isotopic ratios $^{12}C/^{13}C$ and $^{14}N/^{15}N$ can be retrieved from individual rotational lines of the violet band (Manfroid et al. 2009; Bockelée-Morvan et al. 2015; Moulane et al. 2023). The carbon ratio is set primarily by stellar nucleosynthesis and Galactic chemical evolution, while the nitrogen ratio records the UV environment and radial location within the natal protoplanetary disk where the nitrogen-bearing ices were assembled. Together, these isotopic ratios trace both the Galactic chemical evolution and the local formation environment of the parent body; for comprehensive reviews we refer the reader to Füri & Marty (2015) and Romano (2022).

After hydrogen, oxygen is the second most abundant element in comets, present mainly in the form of CO, CO_2, and H_2O. In the optical, oxygen is observable through the forbidden lines arising from the metastable $O(^1D)$ and $O(^1S)$ excited states. The 5578 Å green line is sensitive to the combined contribution of CO, CO_2, and H_2O, whereas the red doublet at 6302 and 6365 Å is driven primarily by H_2O photodissociation (Festou & Feldman 1981; Fink & Johnson 1984; Combi & McCrosky 1991). Because H_2O and CO_2 have no electronic transitions accessible at optical wavelengths, and their rotational and vibrational bands fall in spectral regions affected

⋆ Corresponding author: baltasarluco@uc.cl

by strong telluric absorption, both molecules are difficult to detect directly from the ground. As a consequence, the green-to-red flux ratio (G/R) of the forbidden oxygen lines has been established as an indirect proxy for the CO_2/H_2O ratio in the coma (e.g., Decock et al. 2013; McKay et al. 2015), which in turn evolves with heliocentric distance owing to the different sublimation temperatures of these molecules (152 K for H_2O and 72 K for CO_2). A practical complication when measuring the cometary [O I] lines is contamination by telluric oxygen emission. At sufficient spectral resolution, however, the cometary and telluric components can be cleanly separated thanks to the geocentric velocity of the comet (e.g., Moulane et al. 2023); the 5578 Å line can additionally be blended with C_2 features, a degeneracy likewise resolvable at high resolving power.

Many other molecules have been identified in comets, each providing key diagnostic information. Carbon-chain species, for instance, can emit strongly at visible wavelengths; although their chemistry is still under study, they are useful probes of the coma as daughter species of parents such as C_2H_2 (Pierce & Cochran 2021). Comets have also been classified as carbon-chain depleted or rich (A'Hearn et al. 1995), a distinction thought to reflect the primordial composition of the region in which they formed. Other relevant species include CH, part of the hydrogen-bearing carbon chemistry, and NH_2, an important nitrogen-bearing molecule whose ortho-to-para ratio can serve as a temperature tracer (Kawakita et al. 2004). More recently, Fe and Ni have been detected in comets even at large heliocentric distances (Manfroid et al. 2021), opening the study of Fe- and Ni-carbonyl chemistry. Many further species and applications remain to be explored. In all cases, robust characterization requires long-term monitoring, sufficient signal-to-noise, and if possible spectral resolution high enough to separate lines of the same or different species, so that emission is captured at high fidelity.

The existence of interstellar objects (ISOs) traversing the Solar System has long been predicted as a natural consequence of planetesimal ejection during planetary system formation (McGlynn & Chapman 1989; Jewitt 2003), and they offer a unique opportunity to study the chemistry of their parent system. The discovery of 1I/'Oumuamua on October 19, 2017 (Meech et al. 2017), confirmed this prediction, but the first ISO proved difficult to characterize: with a strongly hyperbolic orbit ($e \approx 1.2$) and an unusual elongated morphology, 1I displayed no detectable coma or gas emission despite intensive observational campaigns, and only upper limits could be placed on the production rates of CN, C_2, and C_3 (Ye et al. 2017). Non-gravitational acceleration along its trajectory hinted at outgassing below detection thresholds (Micheli et al. 2018), but the absence of observable volatiles, combined with the post-perihelion timing of its discovery, precluded any compositional characterization of its ices (Fitzsimmons et al. 2018; 'Oumuamua ISSI Team et al. 2019).

The second confirmed ISO, 2I/Borisov, discovered on August 30, 2019 (Borisov & Minor Planet Center 2019), provided the first opportunity for detailed spectroscopic study of interstellar cometary material. 2I/Borisov developed an active dust coma and was discovered well before its perihelion at q = 2.0 au, enabling a comprehensive monitoring campaign. Optical spectroscopy detected CN at $r_h = 2.7$ au (Fitzsimmons et al. 2019), followed by C_2 (Lin et al. 2020), [O I] (McKay et al. 2020), OH (Xing et al. 2020), NH_2 (Bannister et al. 2020), and exceptionally high CO abundances (Bodewits et al. 2020; Cordiner et al. 2020). The detection of atomic nickel and iron vapor in 2I/Borisov (Opitom et al. 2021) expanded the inventory of detected species, unusual at the time, but rapidly recognized as ubiquitous in solar-system comets (Manfroid et al. 2021; Bromley et al. 2021). Overall, 2I/Borisov appeared broadly similar to solar-system comets in its gas and dust properties, though it showed distinctive compositional features such as a high CO abundance. Neither 2I/Borisov nor 1I/'Oumuamua, however, benefited from a multi-night monitoring campaign spanning both pre- and post-perihelion phases, and 1I/'Oumuamua lacked detectable molecular emission altogether.

3I/ATLAS was discovered on July 1, 2025, by the Asteroid Terrestrial-impact Last Alert System (ATLAS; Tonry et al. 2018) at a heliocentric distance of $\sim$ 4.5 au, on an incoming strongly hyperbolic trajectory with eccentricity $e \approx 6.14$ (Denneau et al. 2025; Seligman et al. 2025; Hopkins et al. 2025). The early discovery, several months before perihelion on October 29, 2025 (q = 1.356 au), enabled an unprecedented multi-facility campaign spanning ground- and space-based observatories. Initial spectroscopy revealed a red, dust-dominated coma reminiscent of D-type asteroids and Trans-Neptunian Objects (Opitom et al. 2025; Puzia et al. 2025; Seligman et al. 2025), with subsequent detections of CN and Ni I emission evolving rapidly as 3I/ATLAS approached the Sun (Rahatgaonkar et al. 2025). Near-infrared spectroscopy with the James Webb Space Telescope (JWST) revealed a coma unusually rich in CO_2 and CO relative to water (Cordiner et al. 2025; Belyakov et al. 2026); SPHEREx, however, placed the CO_2 and CO abundances of 3I/ATLAS as elevated but consistent with those of long-period solar-system comets (Lisse et al. 2026). During the pre-perihelion phase, the absence of detectable C_2 and C_3 placed 3I/ATLAS among the most carbon-chain depleted comets known (Salazar Manzano et al. 2025; Rahatgaonkar et al. 2025), a classification that was subsequently revised following post-perihelion detections of carbon-chain species, bringing 3I/ATLAS back into broad agreement with solar-system comets (Kawakita et al. 2026). The detection of atomic nickel without accompanying iron (Rahatgaonkar et al. 2025) pointed to a carbonyl parent species as the driver of Fe and Ni chemistry in comets, and Hutsemékers et al. (2026) further showed that this mechanism causes the Ni/Fe ratio to converge toward the Solar System trend at decreasing heliocentric distances. Together, these findings highlight the strong time dependence of cometary spectroscopic signatures and underscore the importance of monitoring the volatile evolution of comets, especially ISOs. 3I/ATLAS thus provides a foundation for, and a benchmark against, all future interstellar object studies.

In this paper, we present VLT/ESPRESSO high-resolution spectroscopy ($R \simeq 140\,000$) of the interstellar comet 3I/ATLAS, obtained at heliocentric distances $r_h = 1.67 - 2.45$ au across both the pre- and post-perihelion branches of its orbit. We report:

1. The heliocentric evolution of the CN production rate Q_{CN} across 22 epochs, including a discussion of the observed scatter in the context of both systematics and physical processes that may drive it.
2. The detection and modeling of the three forbidden [O I] lines at 5578, 6302, and 6365 Å with simultaneous two-component (telluric + cometary) Voigt profiles, yielding the green-to-red ratio (G/R), an indirect CO_2/H_2O proxy, and per-epoch radial velocities at the level of hundreds of m s^{-1}.
3. The identification of emission features, including atomic nickel and iron lines and molecular bands of CH and C_2, with comparisons between pre- and post-perihelion stacks and between nucleus-centered and offset coma sightlines.
4. The public release of CometSpec, a Python package for cometary fluorescence modeling and Monte Carlo Markov

chain (MCMC) fitting, incorporating rotational-collisional coupling, MCMC parameter estimation, isotope modeling, and support for arbitrary user-supplied line lists for other molecular species.

The paper is organized as follows. Section 2 describes the observations and observing strategy. Section 3 details the data reduction, including sky subtraction, telluric-line masking, stacking, and continuum modeling. Section 4 presents the CN fluorescence modeling and fitting, the derivation of production rates, the forbidden oxygen line analysis, the wavelength-calibration cross-check, and the broader emission-line inventory. Section 5 discusses the heliocentric evolution of Q_{CN}, the G/R ratio and the implied CO_2/H_2O trend. Section 6 summarizes our conclusions and outlines future directions. Section 7 provides the links to our data and software, and the Appendix provides additional detail on CometSpec and complementary analysis.

2. Observations

This work uses the high-resolution spectrograph ESPRESSO at ESO's 8.2 m Very Large Telescope (VLT) on Cerro Paranal in Chile (Pepe et al. 2021). We observed the interstellar comet 3I at heliocentric distances $r_h = 1.67 - 2.45$ au as part of an ESO Director's Discretionary Time program (Prog. ID 115.29J6, PI: Puzia). The observations were carried out with the High Resolution setup, which provides a resolving power of $R \simeq 140\,000$ in the wavelength range 380–788 nm. The main fiber (A; 1″ diameter) was centered on the comet nucleus, while the second fiber (fiber B) was used in SKYMODE. Fiber B is radially separated by 7″ on the sky from the main fiber, and, in the case of 3I, samples the coma of the comet, rather than blank sky. Because ESPRESSO can use any available VLT unit telescope (UT), the position angle of fiber B on the sky depends on which UT was used for a particular epoch. As there is no derotator, fiber B rotates on the sky during the exposures around fiber A. The physical radius range at the r_h distances of 3I, covered by fiber A, spans $\sim 653 - 932$ km from the comet's nucleus, and fiber B is positioned at a projected nucleocentric distance of $\sim 9\,140$–$13\,050$ km. As fiber B does not provide a pure sky background, separate sky observations were taken interleaved with the science exposures, ensuring that the sky frames were obtained as close in time as possible to the science observations. However, as the airmass of 3I increased through September, the number of sky observations was reduced to prioritize the acquisition of science flux, first to a single sky frame and eventually to no dedicated sky acquisition[1]. To guarantee good tracking and fiber-A centering, we performed reacquisition of 3I in-between observation blocks.

The journal of observations is provided in the Table E.1, where we also summarize some relevant comet parameters extracted from the Jet Propulsion Laboratory's (JPL) Horizons System[2]. Due to technical issues, the night of September 21 was discarded from the analysis. In addition, we removed one exposure taken on September 9 due to star contamination and discarded one exposure from the December 6 run due to bad observing conditions.

[1] In this work we focus exclusively on emission features, not on the reflectance spectrum. At ESPRESSO's spectral resolution, telluric emission lines can be identified and masked even on nights without dedicated sky exposures. The absence of sky frames, therefore, does not affect our analysis and results.

[2] https://ssd.jpl.nasa.gov/horizons/

3. Data reduction

We used the standard ESOREFLEX recipes (Freudling et al. 2013) to reduce the data, adopting the default parameters and the standard calibration frames. After the initial reduction, we used the telluric-corrected (H_2O only) and flux-calibrated output of the pipeline as our 3I fiber A spectrum ($F^A_{3I} = F^A_{total} - F^A_{telluric}$), without the default sky-subtraction option which is normally the flux in fiber B (F^B_{total}). The pipeline does not output the reduced flux from fiber B (F^B_{3I}). We, therefore, recovered 3I's fiber B spectra, using the default sky-subtraction option for fiber A switched on ($F^A_{total} - F^B_{total}$), in the following way:

$$F^B_{3I} = F^A_{3I} - (F^A_{total} - F^B_{total})$$

From these spectra the first step was to ensure precise wavelength calibration. We performed a Gaussian (plus constant) Levenberg-Marquardt least-squares (LS) fit to the [O I] 5578.8955 Å sky line (vacuum reference value from Hanuschik 2003) and forced the solution to be centered at this value using a velocity correction. This procedure was applied only to fiber A. Since fiber B shares the wavelength solution of the main fiber, this and any subsequent wavelength correction were derived from fiber A and then applied to fiber B. Additionally, since this sky line in our observations tends to be stronger than the corresponding cometary line and, combined with the high resolving power and a good initial wavelength solution, the use of a single Gaussian fit to this feature achieved the accuracy and precision within the range needed to compare the spectra taken on different nights. This is demonstrated a posteriori by a cross-check based on the three forbidden [O I] lines, modeled with a two-Voigt fit after applying all wavelength corrections (see Sect. 4.5).

At the resolution of ESPRESSO, the spectral flux density of the sky continuum emission is weak. For nights with dedicated sky exposures, the sky was modeled as a first-order polynomial using a variance-weighted linear least-squares fit with iterative sigma clipping (three iterations at $\sigma = 3$). For science exposures on those nights, sky subtraction was performed using the closest sky exposure in time. We model the continuum flux following Rahatgaonkar et al. (2025) with two adaptations. First, we fix the heliocentric velocity to the ephemeris value obtained from JPL Horizons. Second, we use the Kurucz solar irradiance (Kurucz 2005)[3] instead of a solar analog. We emphasize, however, that at our resolution, lines are sufficiently resolved to model the sky and the reflectance continuum jointly and do not affect the measured line fluxes. We analyze several stacked spectra: (i) per-night stacks; (ii) full pre-perihelion stacks; (iii) full post-perihelion stacks; (iv) three-latest pre-perihelion epoch stacks; and (v) three-earliest post-perihelion epoch stacks[4].

Telluric absorption and sky emission lines do not significantly affect the emission lines analyzed in this work. Nevertheless, our final data products include spectra with identified sky emission lines masked.

The spectra were shifted to the comet rest frame using the geocentric velocity $\dot{\Delta}$ (at the observatory) and then stacked on a per-night basis. For each night, all spectra were linearly interpolated onto the wavelength grid of the first comet exposure of that night (tests with alternative interpolation schemes produced only minimal changes). The stacking was performed with a variance

[3] http://kurucz.harvard.edu/sun/IRRADIANCE2005/

[4] These stacks were produced following the same procedure, with the difference that the continuum/Kurucz irradiance in each stack was computed as the weighted mean of the continua/Kurucz irradiance of the individual nights stacks, all interpolated to the same wavelength grid.

weighted mean with a 5σ clipping of three iterations to exclude as many bad pixels as possible, and only wavelength points with at least two valid contributors were retained. The error of the stacked spectrum was obtained by Gaussian propagation of the individual uncertainties. Bad pixels are strongly down-weighted by the variance weighting and, although some may remain, they do not affect our analysis.

By applying this procedure we obtained, for each night, a final data product consisting of the per-night stacked flux and error spectrum in the wavelength restframe of the comet, a spectrum with the number of exposures contributing to each wavelength point, another flux and error spectrum with the number of contributors after masking telluric lines, the modeled continuum, the modeled reflectance, and the Kurucz solar irradiance spectrum shifted accordingly to the comet restframe. The products are publicly available[5]. We emphasize that the reflectance values obtained with this methodology are meaningful only for nights on which a sky observation was obtained.

4. Analysis

4.1. CN modeling

We developed a Python package for fluorescence modeling, CometSpec, which broadly follows the prescriptions by Manfroid et al. (2009) and Bromley et al. (2024) and is publicly available on GitHub[6]. The key ingredients required to build a fluorescence model are (i) the solar irradiance spectrum responsible for inducing radiative transitions between molecular states and (ii) the set of spectral lines to be considered in the model.

For the solar irradiance, we use the high-resolution spectrum from the latest Kurucz solar irradiance compilation. This spectrum has a wavelength sampling of approximately 0.005 nm and covers the wavelength range $\sim 300-1000$ nm. The irradiance is scaled to the heliocentric distance of the comet and Doppler-shifted according to its heliocentric velocity, for each observing night, in order to account for the Swings effect. Lines beyond the provided solar irradiance are excluded by CometSpec, so for our CN fit only lines in the range $\sim 300-1000$ nm are included. It is important to highlight that solar UV variability affects the photodissociation (Cochran & Schleicher 1993; Huebner & Mukherjee 2015), hence the production rates in comets. Therefore, the assumption of constant solar irradiance constitutes a systematic source of error, with no standard calibration procedure or solar monitoring to control for it.

For the spectral lines, we adopted the isotopologue line list provided by Brooke et al. (2014) for $^{12}C^{14}N$ and from Sneden et al. (2014) for $^{13}C^{14}N$ and $^{12}C^{15}N$. Our analysis includes the $^{12}C^{14}N$ contributions of the $B^2\Sigma-X^2\Sigma$ ($\Delta v=0$; violet) system and the $A^2\Sigma - X^2\Sigma$ ($\Delta v = 1$; red) system. For the latter, we consider the $\Delta v=1$ transitions only, since the inclusion of the $A^2\Sigma - X^2\Sigma$ ($\Delta v=0,2$) systems does not affect our fitted column densities, as we discuss in Sect. 4.2. However, only the violet system is fitted in our analysis, which is the only one that lies within the ESPRESSO wavelength coverage.

These line lists provide all the information required to construct the fluorescence model. Nevertheless, CometSpec also allows the user to supply a custom line list. In this case, each line must include the wavelength, the Einstein spontaneous emission coefficient A_{ul}, an upper-state identifier, a lower-state identifier (which together define a unique transition, e.g., the notation "21" for a transition from level 2 to level 1 in atomic systems), and the statistical weights of the upper and lower levels, g_u and g_l. If rotational collisions are to be included, CometSpec also requires the lower electronic state, lower vibrational state, lower rotational quantum number J, lower-state symmetry (including the F level and parity), and the energy of the lower state. This information ensures a unique identification of each transition and allows the computation of the energy difference ΔE_{ul} between rotational levels.

Once all ingredients are specified, the fluorescence model is constructed by solving the system of Einstein rate equations. We define the population vector

$$x \equiv \begin{pmatrix} n_1 & n_2 & \dots & n_N \end{pmatrix}^T,$$

where n_i is the fractional population of level i, and N is the total number of energy levels included in the model. The total transition rate P_{ij} from level i to level j is defined as

$$P_{ij} \equiv R_{ij} + C_{ij},$$

where R_{ij} represents radiative rates and C_{ij} collisional rates. The radiative rates are given by

$$R_{lu} = B_{lu} J_\nu,$$

i.e., absorption ($l \rightarrow u$), and

$$R_{ul} = A_{ul} + B_{ul} J_\nu,$$

spontaneous and stimulated emission ($u \rightarrow l$). Here, A_{ul} is the Einstein coefficient for spontaneous emission, B_{ul} and B_{lu} are the Einstein coefficients for stimulated emission and absorption, respectively. $J_\nu(\nu_{ul})$ is the mean intensity of the radiation field evaluated at the transition frequency ν_{ul} (obtained from the solar irradiance seen by the comet), and ν_{ul} is the transition frequency, i.e., the line frequency.

The collisional rates are related through:

$$g_l\, C_{lu} = g_u\, C_{ul}\, \exp\left(-\frac{E_u - E_l}{kT_{\rm kin}}\right),$$

where E_u and E_l are the energies of the upper and lower levels involved in collisional coupling[7], respectively, g_u and g_l their statistical weights, k is the Boltzmann constant, and $T_{\rm kin}$ is the kinetic temperature. Note that $T_{\rm kin}$ here is not a thermodynamic temperature as CN is not necessarily in thermodynamic equilibrium; here only statistical equilibrium is assumed, including radiative and collisional processes, so $T_{\rm kin}$ should be taken as the velocity that characterizes the distribution of the colliding particles (Manfroid et al. 2009).

The time-dependent equation for each level i, and assuming fluorescence equilibrium, is

$$\frac{dn_i}{dt} = \underbrace{\sum_{j\neq i} n_j P_{ij}}_{\text{into } i} - \underbrace{n_i \sum_{j\neq i} P_{ji}}_{\text{out of } i} = 0.$$

The indices i and j run over energy levels in the model, not just those connected by observed transitions. The system of equations couples combinations of levels found in the line list, with

[5] https://zenodo.org/records/20966879
[6] https://github.com/baltasarluco/CometSpec
[7] Note that $E_u - E_l$ need not correspond to an observed emission-line frequency, since collisional coupling also connects levels with forbidden or otherwise unobserved radiative transitions.

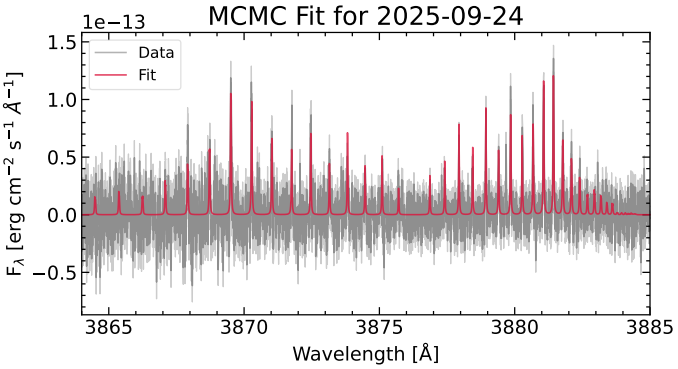

Fig. 1: Spectrum fit of 3I's violet CN band for the night of September 24. The gray line shows the observed data with the shaded light gray region indicating the uncertainty. The red line represents the CN fluorescence model.

some pairs connected only by collisions, some only by radiative processes, and some by both. This system can be written in matrix form as

$$Mx = b, \qquad b \equiv \begin{pmatrix} 1 & 0 & \dots & 0 \end{pmatrix}^T .$$

The matrix M is defined as:

$$M = \begin{pmatrix} 1 & 1 & \cdots & 1 \\ R_{21} + C_{21} & -\sum_{k\neq 2}(R_{k2} + C_{k2}) & \cdots & R_{2N} + C_{2N} \\ \vdots & \vdots & \ddots & \vdots \\ R_{N1} + C_{N1} & R_{N2} + C_{N2} & \cdots & -\sum_{k\neq N}(R_{kN} + C_{kN}) \end{pmatrix}.$$

Along each row i, the off-diagonal elements M_{ij} ($j \neq i$) are the rates *into* level i from level j, while the diagonal element M_{ii} is the (negative) total rate *out of* level i. Replacing the first row of the matrix by unity and setting the first element of b equal to 1, imposes the normalization condition $\sum_i n_i = 1$, as in Magnani & A'Hearn (1986) and Bromley et al. (2021).

The inclusion of the collisional rates C_{ul} introduces a large number of free parameters, following Manfroid et al. (2009). We, therefore, assume $\log C_{ul} \equiv f_{\rm col}$ (with a single $f_{\rm col}$ value) and restrict collisional transitions to those with $\Delta J = 0, \pm 1$. Together with the solar irradiance, the spontaneous emission coefficients A_{ul}, and the Einstein coefficient relations, these provide a complete set of ingredients to formulate the system of equations, which are solved numerically using a least-squares approach. We assume an optically thin coma both for the incoming solar irradiance and for the emitted fluorescence.

In summary, with (i) the solar irradiance spectrum at a given heliocentric velocity and heliocentric distance, (ii) a provided or default line list, and (iii) parameters such as fiber geometry, column density ($\log N$), line spread function (LSF), $f_{\rm col}$ and $T_{\rm kin}$ (if collisions are included), CometSpec allows the computation of a fluorescence emission model of one or multiple isotopologues. See App. A for more details on the computation of uncertainties.

4.2. CN fitting

In this work, we model the CN emission of the $B^2\Sigma$–$X^2\Sigma$ ($\Delta v = 0$; violet) line system and fit the free parameters kinetic temperature $T_{\rm kin}$, the collision transition probability $f_{\rm col}$, the column density $\log N$, the full width at half maximum (FWHM_L) of the Lorentzian profile LSF, and a velocity shift Δv to account for residual mismatches between the observed lines and the ones from Brooke et al. (2014). The uniform priors on all parameters were $\log N \in [5, 20]$, $f_{\rm col} \in [-8, 1]$ where the collisional rate is in units of s^{-1}, $T_{\rm kin} \in [10, 1\,000]$ K, $\mathrm{FWHM}_L \in [0.001, 0.03]$ Å, $\Delta v \in [-1, 1]$ km s^{-1}. All lines with $A_{ul} < 10^4$ were filtered out, which makes the fitting and modeling substantially faster. Throughout, CometSpec assumes input wavelength in Å and flux densities in erg s^{-1} cm^{-2} Å^{-1}.

The MCMC was run with a total of 30 walkers for 5 000 steps, sampling a parameter space of dimension five, producing 750 000 iterations in total. We applied the additional selection of the posterior samples (see App. A). Fig. 1 shows an example of the fitting for the night of September 24, an the posterior distributions can be found in Fig. A.1. Five aspects are worth pointing out from our fits. First, the line profile is not perfectly described by the model, so fitted lines can appear shallower due to a broader base, reflected as a correlation between $\log N$ and FWHM_L. Second, the relative line heights can deviate from the model, either because the Kurucz spectrum does not perfectly reproduce the solar irradiance at the time of observation, or because of assumptions built into the fluorescence model (e.g., the A_{ul} filtering). Third, the inclusion of collisions was essential for reproducing the observations with our adopted line set and filter configuration, as fits that neglected collisions showed significant discrepancies with the data. To assess whether this result was driven by the limited set of transitions included in the model, we performed an additional test of fitting three nights with good S/N, by lowering the minimum A_{ul} threshold to 10, extending the original set of systems included to $B^2\Sigma$–$X^2\Sigma$ ($\Delta v = 0$; violet), the $A^2\Sigma - X^2\Sigma$ ($\Delta v = 0, 1, 2$; red) and the rovibrational transitions in the $X^2\Sigma^+$, and using the extended near-IR solar spectrum of Bromley et al. (2024), for this test we decreased the iterations of the MCMC to 50 000. Under these conditions, the fitted values of $f_{\rm col}$ decreased (at the cost of high computational time), indicating that part of the collisional excitation inferred in the reference model was compensating for the omission of transitions that contribute to the population of the violet system. Despite this reduction in $f_{\rm col}$, the retrieved column densities remained largely unchanged between the two model configurations; the analysis is therefore unaffected, although $f_{\rm col}$ itself should be interpreted with caution. Fourth, for some nights, the posterior distribution of $f_{\rm col}$ in both the reference and IR-extended models exhibited a regime in which further increases in the collisional rate produced negligible changes in the predicted spectrum. This behavior suggests that, beyond a certain threshold, collisions effectively thermalize the rotational population within the ground vibrational state. Fifth, deviations from the fits can also be explained if other excitation pathways, in addition to fluorescence, are considered. The fits and corner plots for all observing nights can be found online[8].

4.3. Production rates

CometSpec can also compute production rates, using standard Haser-model procedures (Haser 1957). The required inputs are the fluorescence model (specifically the fitted column density), the gas outflow velocity, the parent and daughter scale lengths, and the aperture geometry. The spatial distribution is integrated within the aperture using sbpy (Mommert et al. 2019), assuming the aperture is centered on the nucleus. We consider two sources

[8] https://zenodo.org/records/20966879

of uncertainty on Q_{CN}: a statistical error from the MCMC fit and a systematic error from slit-losses.

The statistical error is obtained by propagating the column-density posterior chain into a production-rate chain and taking half the difference between the 84th and 16th percentiles. The slit-loss systematic accounts for flux that falls outside the fiber aperture under varying observing conditions. Given the minimum and maximum seeing and target altitude during a given night, together with a reference wavelength and the aperture geometry, we estimate the corresponding range of sky point spread function (PSF) FWHM following Persson (2022). Assuming a two-dimensional Gaussian PSF, we then compute the fraction of flux falling outside the aperture at each extreme, which maps directly into a range of inferred production rates via column densities ($Q_{CN} \propto N \propto F$). The slit-loss error is defined as the mean of the absolute deviations of the nominal Q_{CN} from these two extrema. The total uncertainty on Q_{CN} is the quadrature sum of the statistical and systematic contributions.

We adopt solar-system cometary scale lengths in the absence of 3I-specific constraints. Therefore, the derived Q_{CN} values should be taken as relative rather than absolute, and direct comparison with Rahatgaonkar et al. (2025) is only valid to the extent that both works make the same assumption. Here we assume an outflow velocity of $v = 0.85 \times r_h^{-0.5}$ km s^{-1} (Cochran & Schleicher 1993) and the parent scale length of 1.3×10^4 km and daughter scale length of 2.1×10^5 km scaled by r^{-2} at 1 au (A'Hearn et al. 1995). We stress, however, that 3I has an unusually CO_2- and CO-rich coma where the outflow dynamics may differ. For instance, Cordiner et al. (2026) measured an HCN outflow velocity of $v = 0.276 \pm 0.015$ km s^{-1}, lower than the 0.551 km s^{-1} expected from the Cochran & Schleicher (1993) relation at the corresponding heliocentric distance; adopting the latter would yield a production rate twice as high as the one derived from the Cordiner et al. (2026) velocity. Similarly, the HCN → CN scale lengths from A'Hearn et al. (1995) assume solar-driven HCN photodissociation rates, which is likely appropriate for 3I, but should be kept in mind as a potential systematic.

For the nights of September 2, 3, 8, and December 21, CN was not clearly detected, and we instead derived 50%-completeness upper limits as follows (Fig. 2). For each night, we generated 50 synthetic spectra matching the observed signal-to-noise conditions, spanning a range of injected CN column densities. Each realization was fitted with an MCMC procedure analogous to that described above, with three simplifications: the iterative posterior filter was disabled, we used 6 000 iterations per fit, and only $\log N$ was left free, with a broad uniform prior. All the other parameters were set to a first fit of the few lines detected each night, that followed the same procedure explained in Sect. 4.2. A recovery was counted as successful when (i) the injected column density fell within the 1σ uncertainty interval of the recovered value and (ii) the relative uncertainty on N was below 10%. The recovery fraction at each injected column density is then the number of successful recoveries divided by 50. We converted the injected column-density grid into production rates and defined the upper limit as the interpolated Q_{CN} value at which the recovery fraction first drops to 50%; the slit-loss error was included. Table E.2 reports the resulting $\log Q_{CN}$ for each non-detection and detection night.

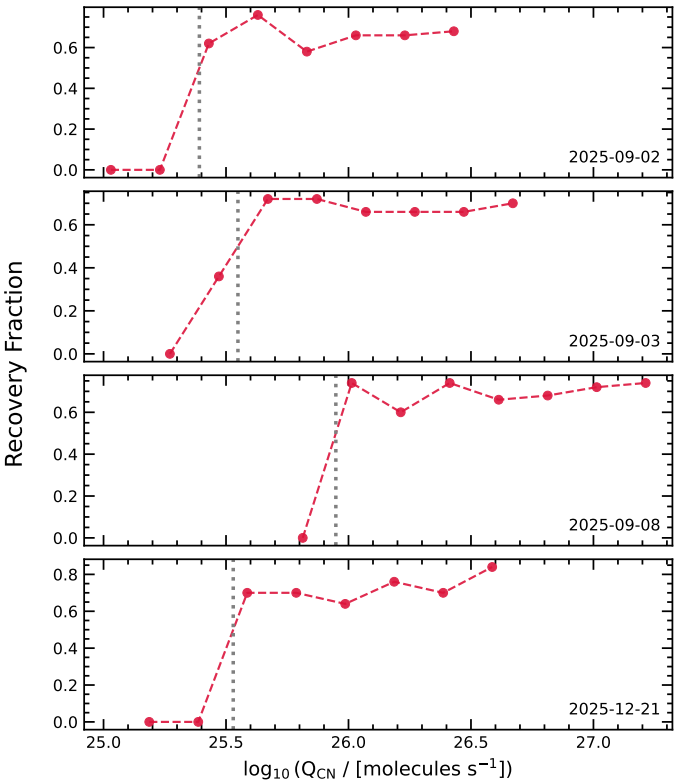

Fig. 2: Recovery fraction as a function of CN production rate for the nights of September 2, 3, and 8, and December 21. Red points show the values obtained as described in Sect. 4.3, and the red dashed line shows a linear interpolation. The black dotted line indicates the adopted upper limit, as described in Sect. 4.3.

4.4. Forbidden oxygen

Each forbidden oxygen line at 5578, 6302, and 6365 Å was modeled as the sum of two Voigt profiles, one for the telluric component and one for the cometary emission, with the Lorentzian FWHM tied between the two. Rather than fit the lines independently, we fitted them jointly in a single MCMC run over a 21-dimensional parameter space, comprising three shared $FWHM_L$ (one per line), and six values each of $FWHM_G$, the Lorentzian amplitude A_L, and the line center x_0 (one per Voigt component). The sampler was run with 100 walkers for 5 000 steps, totaling 1.05×10^7 iterations, and the iterative posterior filter described in App. A was again applied.

Priors were tuned per night to ensure convergence and were, in some cases, highly restrictive. This does not bias our analysis, since the quantities of astrophysical interest are the line intensities and centers. We prioritized obtaining accurate line profiles, in which both the telluric and cometary components are clearly separated, and accepted larger uncertainties on the remaining (nuisance) parameters in the few highly blended cases where degeneracies dominate.

Figure 3 shows four representative fits of the [O I] 6302 Å line, two pre-perihelion and two post-perihelion. The full set of fits and corner plots is available online[9]. Table E.2 summarizes the main results of the [O I] fits.

4.5. Geocentric radial velocity

The high spectral resolution of ESPRESSO, combined with the data quality, allows clear separation of the telluric and cometary lines on nearly every night. As anticipated in Sect. 3, anchoring

[9] https://zenodo.org/records/20966879

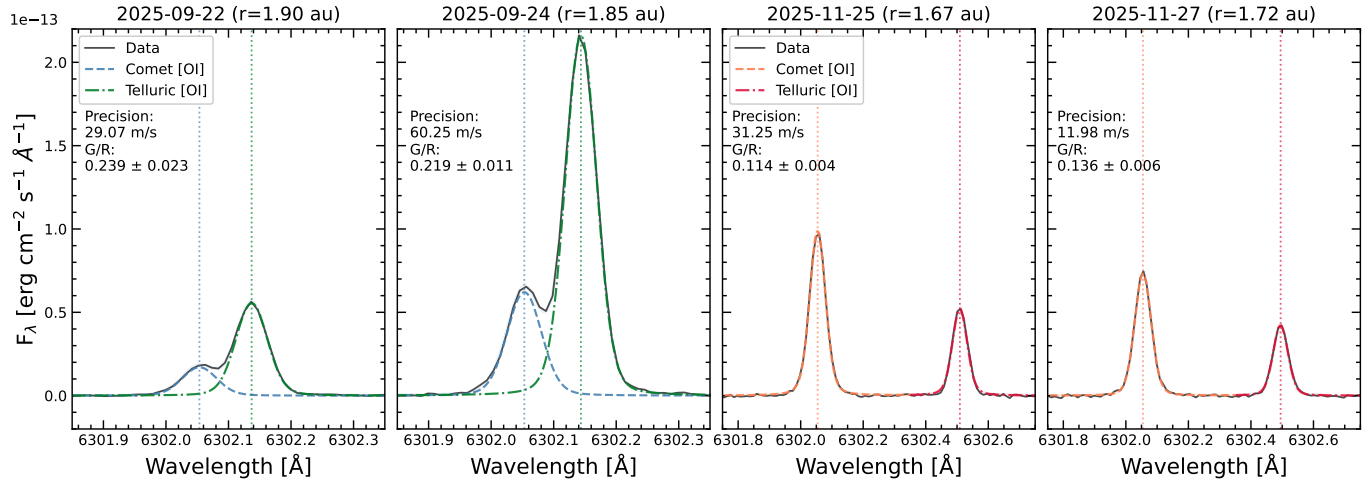

Fig. 3: Fits of the [O I] 6302 Å line for four nights: September 22 ($r_h = 1.9$ au) and 24 ($r_h = 1.85$ au) pre-perihelion (left panels), and November 25 ($r_h = 1.67$ au) and November 27 ($r_h = 1.72$ au) post-perihelion (right panels). The solid black line shows the observed data. The cometary line fit is shown in dashed blue (pre-perihelion) and orange (post-perihelion), while the telluric fit is shown in dot-dashed green (pre-perihelion) and red (post-perihelion). The G/R ratio is indicated in each panel, along with the precision estimated as the difference of $\dot{\Delta}$ estimated from the fit and the ephemeris value.

the wavelength solution to the [O I] 5578 Å telluric line and applying a $\dot{\Delta}$ correction yields sufficient precision for stacking both within and across nights. This is confirmed by the close agreement between the ephemeris velocity and the velocity derived from the cometary-telluric centroid offset. We find that residuals fall below 1 km s^{-1} on all nights and reach $\sigma \simeq 135-228$ m s^{-1}. Figure 4 illustrates this remarkable agreement.

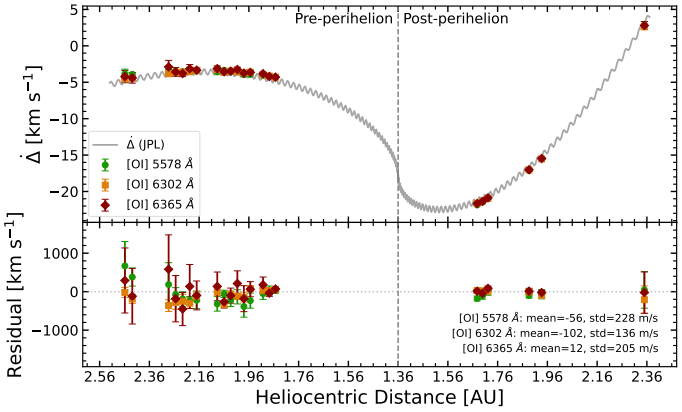

Fig. 4: Geocentric 3I velocity ($\dot{\Delta}$) derived from the forbidden oxygen lines by differencing the cometary and telluric [O I] line centroids. *Upper panel:* per-line measurements, with green circles for [O I] 5578 Å, orange squares for [O I] 6302 Å, and red diamonds for [O I] 6365 Å. The gray line shows the JPL Horizons ephemeris value. *Lower panel:* velocity residuals relative to the ephemeris.

4.6. Emission lines detected

In addition to the violet CN band and the forbidden oxygen lines, the ESPRESSO spectra reveal several additional emission features (see Fig. 5). Atomic iron and nickel lines are identified from the NIST Atomic Spectra Database (Kramida et al. 2024), and molecular features using the cometary emission-line catalog of Cambianica et al. (2021). To characterize the evolution of these features across 3I's perihelion passage and to probe their spatial distribution within the coma, we carry out two comparisons: pre- versus post-perihelion stacked spectra (Fig. 5), and fiber A (nucleus-centered) versus fiber B (projected offset) detections on individual nights (Fig. 6). We also performed a line-stacking search for isotopologues, which yielded no detection (see App. B for details).

4.6.1. Pre- versus post-perihelion evolution

The pre/post comparison reveals two notable changes. First, we find a post-perihelion enhancement of Fe I emission when comparing the spectra in Fig. 5. This difference is mainly explained by the slightly smaller heliocentric distances (∼ 0.17 au) of the post-perihelion observations, which enhance the Fe lines; a direct comparison between nights E17 (1.85 au) and E21 (1.88 au) yields production rates $\log Q_{Fe} = 24.42 \pm 0.06$ and $\log Q_{Fe} = 24.41 \pm 0.08$, respectively (Q in molecules s^{-1}), showing no clear asymmetry, although a robust assessment of the Fe pre/post-perihelion asymmetric behavior predicted by thermal models would require comparing a larger sample of nights, which lies beyond the scope of this work (see Sect. 4.3 for details on the production rate derivation and App. C for the Fe case). When comparing these two values to the ones presented by Hutsemékers et al. (2026) we find that for similar heliocentric distances our values are ∼ 0.3 dex higher. These differences can be explained by a different set of lines used for fluorescence calculations (see App. C for the specific differences between the models), imperfections in the LSF treatment, due to different prescriptions of simultaneous lines fits, centering offsets during observations, or aperture effects since our fiber is smaller than the UVES/X-Shooter slits. Second, C_2 (Swan bands) and CH (4300 Å band) are detected more clearly in the post-perihelion stack than in the pre-perihelion data. From the stack of the first three post-perihelion nights, we derive $\log Q_{C_2}$ in the range of $[25.20, 25.68]$, corresponding to $\log Q_{C_2}/Q_{CN} = [-0.79, -0.10]$ when compared to the mean CN production rate over the same epochs (see App. C and

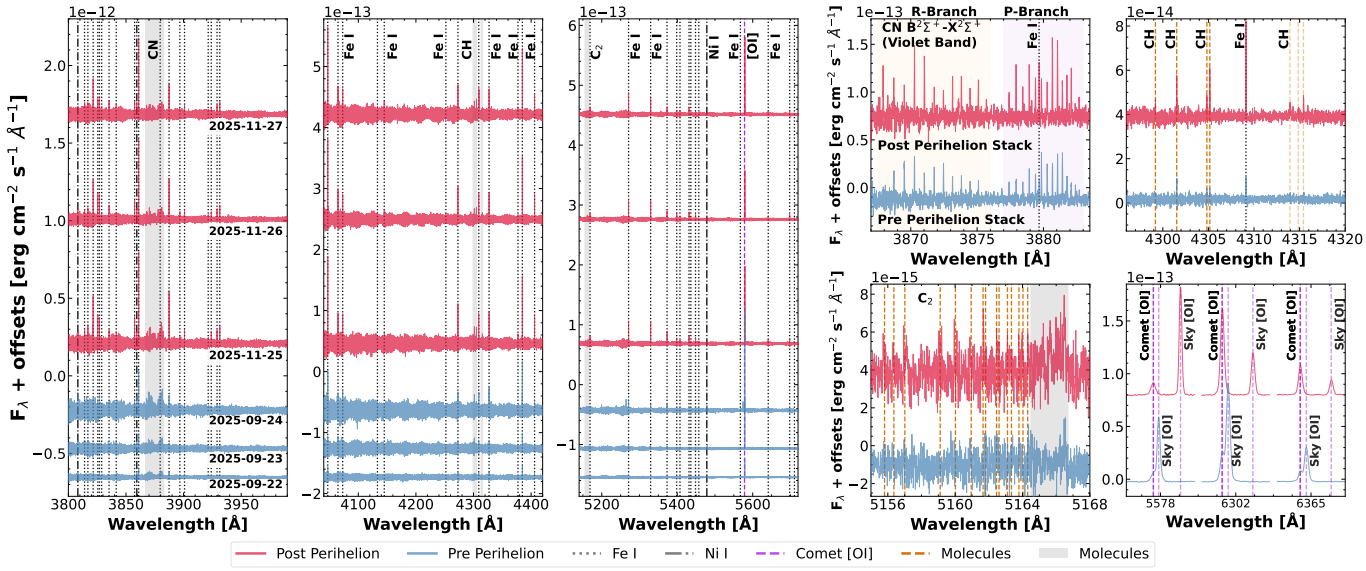

Fig. 5: Detected emission features in the ESPRESSO spectra of 3I/ATLAS for pre- and post-perihelion stacks (blue spectra and red spectra, respectively) using individual spectra from six nights (three pre-perihelion: 2025-09-22, 2025-09-23, 2025-09-24 in blue; three post-perihelion: 2025-11-25, 2025-11-26, 2025-11-27 in red). *Three left columns:* Coverage of the ranges 3800–3950 Å, 4100–4400 Å, and 5200–5700 Å, with spectra offset vertically for clarity. *Two right columns:* pre- and post-perihelion stacks of the same nights, showing the CN $B^2\Sigma^+$–$X^2\Sigma^+$ violet band and its *R*- and *P*-branches (3867–3882 Å), the CH band (4300–4320 Å), the C_2 Swan band (5156–5166 Å), and the three cometary forbidden [O I] lines at 5578, 6302, and 6365 Å alongside their telluric counterparts. In all panels, vertical dashed lines and shaded bands mark the positions of the identified species, labeled in the legend.

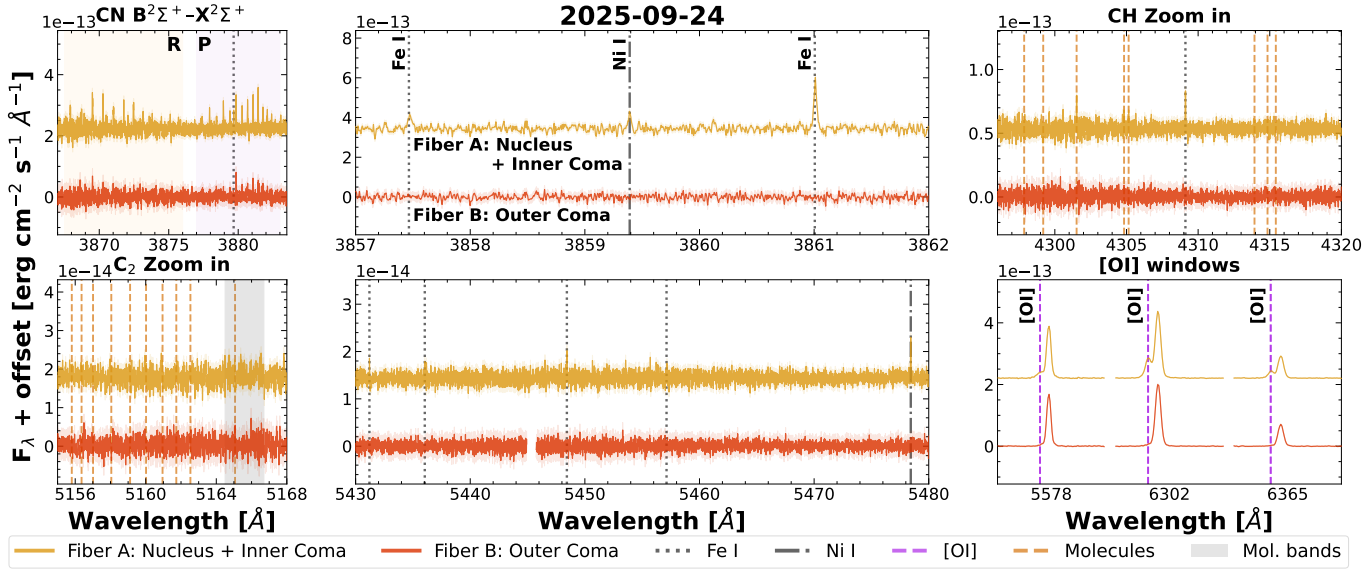

Fig. 6: Comparison of fiber A (nucleus; yellow) and fiber B (coma; orange) spectra obtained on 2025-09-24, covering key spectral regions: the CN $B^2\Sigma^+$–$X^2\Sigma^+$ violet band with its R- and P-branches (3867–3882 Å), Fe I and Ni I lines (3857–3862 Å and 5430–5480 Å), the CH band (4300–4320 Å), the C_2 Swan band (5156–5166 Å), and the three [O I] forbidden lines at 5578, 6302, and 6365 Å; in all panels, vertical dotted, dashed, and dot-dashed lines indicate the positions of Fe I, Ni I, [O I], and molecular lines respectively, with shaded bands marking molecular band regions, as labeled in the legend. On this night, fiber B was placed at ∼12 800 km radial distance from the nucleus.

Sect. 4.3 for details on the line lists used and the fitting procedures for Fe, C_2, and CH). This ratio places 3I within or near the boundary of the carbon-chain-depleted category defined by A'Hearn et al. (1995), where $\log Q_{C_2}/Q_{CN} < -0.18$. Our measurement is broadly consistent with the pre-perihelion classifications of Rahatgaonkar et al. (2025), Salazar Manzano et al. (2025), Lazzarin et al. (2026), and Hutsemékers et al. (2026), although 3I does not appear to represent an extreme case of carbon-chain depletion. Our $\log Q_{C_2}$ values are in agreement with those reported by Kawakita et al. (2026); nevertheless, our range remains consistent with carbon-chain depleted classification. We caution, however, that our C_2 model is subject to high degeneracies, and a systematic underestimation of the associated uncertainties cannot be excluded (see App. C). In addition,

the limit of −0.18 defined by A'Hearn et al. (1995) to classify a comet as C_2-depleted comes from narrow-band photometry, which implies FoVs larger than our fiber; hence aperture effects are another point requiring caution.

For CH, the same post-perihelion stack yields $\log Q_{CH} = 26.38 \pm 0.05$ and $\log Q_{CH}/Q_{CN} = 0.31 \pm 0.12$, both within the range of typical solar-system comets (Cochran et al. 2012).

4.6.2. Spatial systematics from radially offset fiber B

Not every epoch is suitable for the nucleus versus coma (i.e., fiber A versus fiber B) comparison because the position angle of fiber B rotates on the sky between exposures and, depending on which UT is used, more or less coma flux enters fiber B (see Sect. 2). On September 24, 2025, however, both fibers yield significant detections: CN is clearly present in fiber B at a projected nucleocentric distance of ∼ 12 800 km, while Fe I and Ni I emissions are absent at such large nucleocentric distances, consistent with their known origin close to the nucleus (Hutsemékers et al. 2021; Manfroid et al. 2021; Rahatgaonkar et al. 2025; Hutsemékers et al. 2026).

As an independent check on the adopted CN parent scale length, we compared the column density predicted by the Haser model at the projected nucleocentric distance of fiber B (7″) with the column density obtained from a fluorescence fit to the fiber B spectrum (see Sect. 4.2 for fitting details). The Haser prediction yields $\log N/(\text{molecules cm}^{-2}) = 11.31 \pm 0.06$, while the fiber B fit gives $\log N/(\text{molecules cm}^{-2}) = 11.23 \pm 0.07$, in very good agreement. This consistency supports the validity of the adopted HCN–CN scale lengths and outflow velocity to compute the production rates (see Sect. 4.3).

5. Discussion

5.1. CN production rate evolution

We modeled the heliocentric evolution of Q_{CN} with two power laws: a symmetric form $Q_{CN} = a\,(r_h/1\text{ au})^b$ fitted jointly to the pre- and post-perihelion data, and an asymmetric piecewise form $Q_{CN} = Q_{peri}\,(r_h/r_0)^b$ with independent exponents on each branch and continuity enforced at perihelion ($r_0 = 1.36$ au). Both fits were performed in $\log Q_{CN}$ space, minimizing a negative Gaussian log-likelihood with the Nelder-Mead algorithm, performed both with upper limits excluded and with them included as censored data. Best-fit values and 1σ uncertainties correspond to the 16th, 50th, and 84th percentiles of a 10 000-iteration bootstrap Monte Carlo. Figure 7 shows the resulting $Q_{CN}(r_h)$ scaling relations (see Table 1 for fit results) and the fit residuals. The pre-perihelion power-law exponent derived here is shallower than the one reported by Rahatgaonkar et al. (2025). We attribute the difference to four factors: (i) the substantial epoch-to-epoch scatter in Q_{CN}, which broadens the confidence region of the fit; (ii) the absence of detections at our largest sampled heliocentric distances, where only upper limits are available; (iii) the inclusion of slit-loss uncertainties, which were not accounted for by Rahatgaonkar et al. (2025); and (iv) aperture effects. All exponents derived in this work remain within the range observed for solar-system comets (A'Hearn et al. 1995).

We assessed the relative merit of the symmetric and asymmetric CN power-law models using the Bayesian information criterion (BIC). When only detections are included, the asymmetric model is not preferred (ΔBIC = 3.5), primarily because the sparse sampling at large heliocentric distances leaves the post-perihelion branch poorly constrained. When upper limits are included, however, the asymmetric model is mildly favored (ΔBIC = 6.9), consistent with thermal models that predict pre/post-perihelion asymmetries arising from the delayed heating of subsurface layers (Puzia et al. 2025; Yaginuma et al. 2026), a behavior also observed in solar-system comets (Schleicher et al. 1991). However, the pre- and post-perihelion exponents are consistent within errors, which implies that more sampling is needed to robustly confirm the asymmetry. Unexpectedly, the best-fit post-perihelion slope is steeper than the pre-perihelion one. Thermal-lag arguments predict the opposite: residual subsurface heating after perihelion should sustain HCN sublimation and produce a shallower decline in Q_{CN} on the outbound branch. Given that the post-perihelion data are consistent with a single power-law decline and that the limited r_h coverage after perihelion prevents a robust independent measurement of the post-perihelion exponent, we regard this apparent steepening as driven by the sparse sampling rather than by a physical effect. The high bootstrap error of the fitted exponents underscores the importance of dense temporal sampling and sustained monitoring across the full perihelion passage of such objects. We note, however, that all variants of our fit (pre/post-perihelion only or both branches, with or without upper limits) yield exponents that are mutually consistent within their statistical and systematic uncertainties. Two refinements, beyond the scope of the present work, could further improve the CN evolution model: (i) allowing the peak production rate to be offset from perihelion, as has been observed in some solar-system comets (Knight & Schleicher 2013), and (ii) incorporating an explicit temperature dependence through an Arrhenius sublimation term.

The lower panel of Fig. 7 shows substantial scatter in the residuals, indicating that the simple power-law models do not capture the full variability of Q_{CN}. We considered several candidate drivers of this dispersion. Daily variations in the far-ultraviolet (FUV) irradiance cannot be neglected, as they directly affect the HCN photodissociation rate (Huebner & Mukherjee 2015). We integrated the daily irradiance from the Flare Irradiance Spectral Model 2 (FISM2[10]) over the 0.01–100 nm range and find that during our observations the standard deviation is ∼ 10 % of the mean total FUV flux, suggesting that solar UV variability may contribute to the observed scatter. Nucleus rotation (Schleicher et al. 1990) can drive single-period modulation; phase-folding the residuals at the currently published rotation periods of 3I, $P_{rot} = 15.48$ h (Serra-Ricart et al. 2026), 16.16 h (Santana-Ros et al. 2025), or 16.79 h (de la Fuente Marcos et al. 2025), reveals no coherent pattern, and a Lomb–Scargle periodogram of the Q_{CN} residuals shows no significant periodicity within a 24-hour search window; however, we cannot rule out that rotational modulation contributes to the observed scatter at a level below our detection threshold. Localized, spontaneous outbursts could contribute to the scatter; however, resolved photometry will be needed. The solar wind is another plausible contributor, as it could alter the chemical environment within the coma; while cometary response to coronal mass ejection events has been studied in the UV (Noonan et al. 2018; Götz et al. 2024), analogous investigations in the optical relating emission to solar wind velocity, density, and temperature on daily timescales are still lacking; target-of-opportunity campaigns triggered by heliospheric modeling would help fill this gap.

More significantly, systematic effects from the assumed Haser model could lead to under- or overestimation of the production rate. In Fig. 7, we show two lines corresponding to out-

[10] https://lasp.colorado.edu/lisird/data/fism_daily_hr

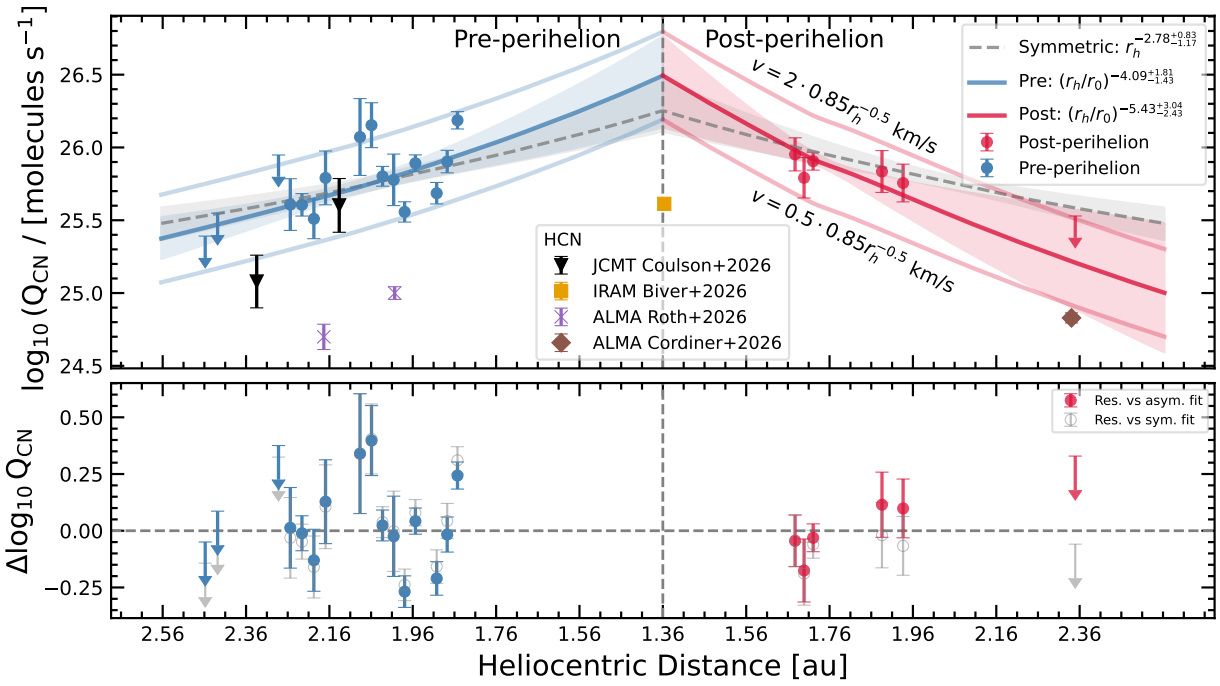

Fig. 7: CN evolution during the ESPRESSO campaign. *Upper panel:* CN production rate Q_{CN} (logarithmic scale) as a function of heliocentric distance r_h. Blue and red symbols denote pre- and post-perihelion measurements, with 1σ error bars and downward arrows for upper limits. The vertical dashed line marks perihelion. The black dashed line and gray band show the symmetric fit $Q_{CN} = a\, r_h^b$ and its 1σ confidence region; the blue and red curves show the asymmetric piecewise fit, with continuity at perihelion, while upper limits are not included in the fit. The two lighter solid lines show the effect of doubling and halving the adopted outflow velocity on the fitted power law, bracketing the systematic uncertainty introduced by the model assumptions. Black triangles, the yellow square, violet crosses, and the brown diamond show HCN production rates from Coulson et al. (2026); Biver et al. (2026); Roth et al. (2026); Cordiner et al. (2026), respectively. *Lower panel:* residuals with respect to the asymmetric fit (filled symbols, color-coded as above) and to the symmetric fit (open gray symbols). The horizontal dashed line marks the zero residual.

Table 1: CN fits of the heliocentric scaling relation $Q_{CN} = a\,(r_h/1\ \mathrm{au})^b$ and $Q_{CN} = Q_{peri}\,(r_h/r_0)^b$

Data included	Upper limits included			Upper limits not included		
	$\log a$	b	$\log Q_{peri}$	$\log a$	b	$\log Q_{peri}$
Both	$26.84^{+0.33}_{-0.22}$	$-3.59^{+0.70}_{-1.01}$	—	$26.62^{+0.37}_{-0.25}$	$-2.78^{+0.83}_{-1.17}$	—
Pre	—	$-4.62^{+1.25}_{-1.22}$	$26.57^{+0.24}_{-0.26}$	—	$-4.09^{+1.81}_{-1.43}$	$26.49^{+0.27}_{-0.35}$
Post	—	$-6.14^{+2.16}_{-2.18}$	$26.57^{+0.24}_{-0.26}$	—	$-5.43^{+3.04}_{-2.43}$	$26.49^{+0.27}_{-0.35}$

Table 2: Power-law fits of the heliocentric scaling relation $F = c\,(r_h/r_0)^a$ for the [O I] forbidden lines.

Parameter	[O I] 5578 Å	[O I] 6302 Å	[O I] 6365 Å
a (Pre)	$-4.52^{+0.74}_{-0.79}$	$-7.22^{+0.84}_{-1.01}$	$-7.33^{+0.74}_{-1.11}$
a (Post)	$-3.35^{+1.35}_{-1.71}$	$-5.51^{+1.43}_{-1.77}$	$-5.67^{+0.99}_{-1.62}$
c (erg cm^{-2} s^{-1})	$(2.24^{+0.96}_{-0.60}) \times 10^{-15}$	$(2.05^{+1.11}_{-0.58}) \times 10^{-14}$	$(7.40^{+3.35}_{-1.62}) \times 10^{-15}$

flow velocities scaled by factors of two and one-half (the latter matching the outflow velocity measured by Cordiner et al. (2026) when $0.85\, r_h^{-0.5}$ is rescaled); relative values remain consistent, suggesting systematics as a plausible cause for differences between datasets and studies. For instance, if the outflow velocity varies with heliocentric distance in a nontrivial manner deviating from $r^{-0.5}$ scaling relation, the elevated production rates could be explained solely by an outflow velocity higher than assumed. It has also been shown that an under- or overestimation of daughter and parent scale lengths can lead to significant production rate differences (Fray et al. 2005). Another potential systematic is the seeing conditions during the night. In our case, the maximum seeing values in each night correlate mildly with the Q_{CN} residuals, albeit without clear statistical significance (Pearson $r = 0.47$, $p = 0.05$). We, therefore, do not consider this a major effect, as it is already incorporated into our analysis via the slit-loss error. Finally, comet miscentering during exposures represents a potential source of scatter. Recentering was required between each exposure, and positional deviations within a single exposure, combined with the direction of drift, could contribute to this effect. To assess this systematic, we examined the continuum evolution and the residuals (see

App. D), which again exhibit significant scatter. All the possible explanations for the high scatter proposed so far need to be analyzed taking into account that the fiber size could also amplify these effects.

Since CN in cometary comae is primarily produced through the photodissociation of HCN, simultaneous optical (CN) and sub-millimeter (HCN) observations are essential to disentangle whether the observed scatter reflects true physical variability in the coma environment or residual systematics. Such coordinated campaigns would additionally clarify whether HCN is the sole parent driving CN production in 3I, or whether additional sources (e.g., CN-bearing grains or other parents) contribute, as has been seen for some solar-system comets (Fray et al. 2005). These considerations should be kept in mind for future interstellar visitor (and comet) observing campaigns, where coordinated multi-wavelength campaigns from discovery onward will be essential to maximize the scientific return from these rare objects. From the literature we retrieved 3I measurements of HCN from three facilities: JCMT (Coulson et al. 2026), IRAM (Biver et al. 2026), and ALMA (Roth et al. 2026; Cordiner et al. 2026); these are all shown in Fig. 7. Comparing these values with our asymmetric fit (without upper limits), and scaling the outflow velocity to that of Cordiner et al. (2026), we find $\log(Q_{CN}/Q_{HCN})$ = 0.15 ± 0.20 and -0.22 ± 0.19 for Coulson et al. (2026), 0.66 ± 0.10 and 0.50 ± 0.07 for Roth et al. (2026), 0.57 ± 0.35 for Biver et al. (2026), and 0.09 ± 0.36 for Cordiner et al. (2026). The values from Coulson et al. (2026) and Cordiner et al. (2026) are consistent with HCN being the dominant parent of CN, whereas those from Roth et al. (2026) and Biver et al. (2026) are not. With the current data and differing analysis methods, we cannot determine which is correct, mainly due to the difficulty of disentangling the effects of aperture, beam size, heliocentric distance, and sparse sampling.

5.2. G/R ratio

We applied the same fitting procedure used for Q_{CN} to each forbidden [O I] line flux, modeling its heliocentric-distance dependence as a piecewise power law, $F = c\,(r_h/r_0)^a$, with independent pre- and post-perihelion exponents and continuity enforced at perihelion. Table 2 summarizes the best-fit parameters and their 1σ uncertainties from the bootstrap experiments.

The results are presented in Fig. 8. The upper panels show the flux of the three forbidden [O I] lines as a function of heliocentric distance, together with the corresponding piecewise-power-law fits and residuals. The lower panels show the green-to-red ratio (G/R) and its residuals; the G/R model and its confidence band are derived from the ratio of the individual line fits, evaluated at each bootstrap iteration to propagate the correlated uncertainties.

The green [O I] 5578 Å line is produced primarily by the photodissociation of H_2O and CO_2, while the red doublet at 6302 and 6365 Å originates predominantly from H_2O (Fink & Johnson 1984; Combi & McCrosky 1991), with a negligible CO contribution (Bhardwaj & Haider 2002). As 3I approaches perihelion and its water production rate rises (see thermal models of Puzia et al. 2025; Yaginuma et al. 2026), the red lines are therefore expected to brighten more steeply than the green line, in agreement with the steeper exponents we measure for the red doublet (Fig. 8, top panel). The residuals about the smooth power-law model (Fig. 8, second panel) follow the same epoch-by-epoch pattern as the CN residuals.

The G/R ratio is known to depend on nucleocentric distance because of the very different radiative lifetimes of the two red O(^{1}D) lines ($\tau \approx 130$ s) and the green O(^{1}S) line ($\tau \approx 0.8$ s; Bhardwaj & Raghuram 2012; Raghuram & Bhardwaj 2014; Decock et al. 2015; Kramida et al. 2024), which translate into very different emission scale lengths in the coma. ESPRESSO's fiber A covers up to a nucleocentric radius of $\sim 650-930$ km around the comet nucleus, and because our fiber radius is larger than the O(^{1}S) and comparable with the O(^{1}D) scale length, we sample the fully integrated emission, so the variations of G/R with nucleocentric distance within the coma are not resolved and all our values are comparable among themselves. Similarly, if we compare with larger fields of view (FoVs), which do not cover the full O(^{1}D) scale length, we expect our values to be larger.

We find that the G/R ratio in 3I decreases steadily with decreasing heliocentric distance (Fig. 8, third panel), in agreement with previous cometary observations (Decock et al. 2013; McKay et al. 2013). All measured G/R values fall within 1σ of the piecewise model (Fig. 8, fourth panel), confirming that the power-law description captures the bulk of the heliocentric trend; this behavior is consistent with thermal-inertia models of the nucleus (Puzia et al. 2025; Yaginuma et al. 2026), in which the delayed subsurface heating causes the CO_2/H_2O production ratio and, therefore, the G/R ratio to decay more gradually after perihelion, owing to the higher sublimation temperature of H_2O relative to CO_2. The comparison with a symmetric fit yields ΔBIC values of $105, 2011, 277$ for [O I] 5578, 6302, 6365 Å, respectively, indicating a clear signal of asymmetry. However, the exponents of the piecewise functions are consistent within their uncertainties, and therefore denser sampling across future cometary perihelion passages will be needed to establish this asymmetry at a statistically meaningful level. Several independent studies have reported an extreme CO_2/H_2O ratio in 3I, with H_2O becoming increasingly dominant as the comet approaches perihelion (Lisse et al. 2025; Cordiner et al. 2025; Shinnaka et al. 2026; Belyakov et al. 2026; Lisse et al. 2026). Our G/R measurements are consistent with these findings: the ratio is elevated relative to solar-system comets at all sampled heliocentric distances (possibly due to the small aperture), and declines steadily toward perihelion as the relative water contribution grows. Notably, our G/R values are comparable to those measured for 2I/Borisov (Opitom et al. 2021), placing both interstellar visitors in a similar region of the G/R-r_h plane, well above the locus of Jupiter-family and Oort-Cloud comets.

We also note that systematic monitoring of Oort-Cloud comets remains scarce, and long-term observational campaigns of such objects entering the Solar System for the first time will be essential for placing future interstellar objects in a broader chemodynamical and Galactic context.

We estimated the CO_2/H_2O ratios following the method of Decock et al. (2013), in which CO is omitted due to its low contribution, as found by the same authors. Using effective production rates from Bhardwaj & Raghuram (2012) and the branching ratio for the green line from Slanger et al. (2006), we obtain values ranging from 0.06 ± 0.01 (r_h = 1.67 au) to 1.06 ± 0.60 (r_h = 2.17 au), see Table E.2. When compared directly with the G/R ratio from Shinnaka et al. (2026), our results are in agreement, with our values slightly higher, as expected from our smaller aperture. For the CO_2/H_2O ratios, our values agree better with the SPHEREx measurements (Lisse et al. 2026) and are smaller than the JWST ones (Belyakov et al. 2026); in particular, one of the JWST data points is inconsistent with our estimated relation (see Fig. 8). This is somewhat counterintuitive: we would

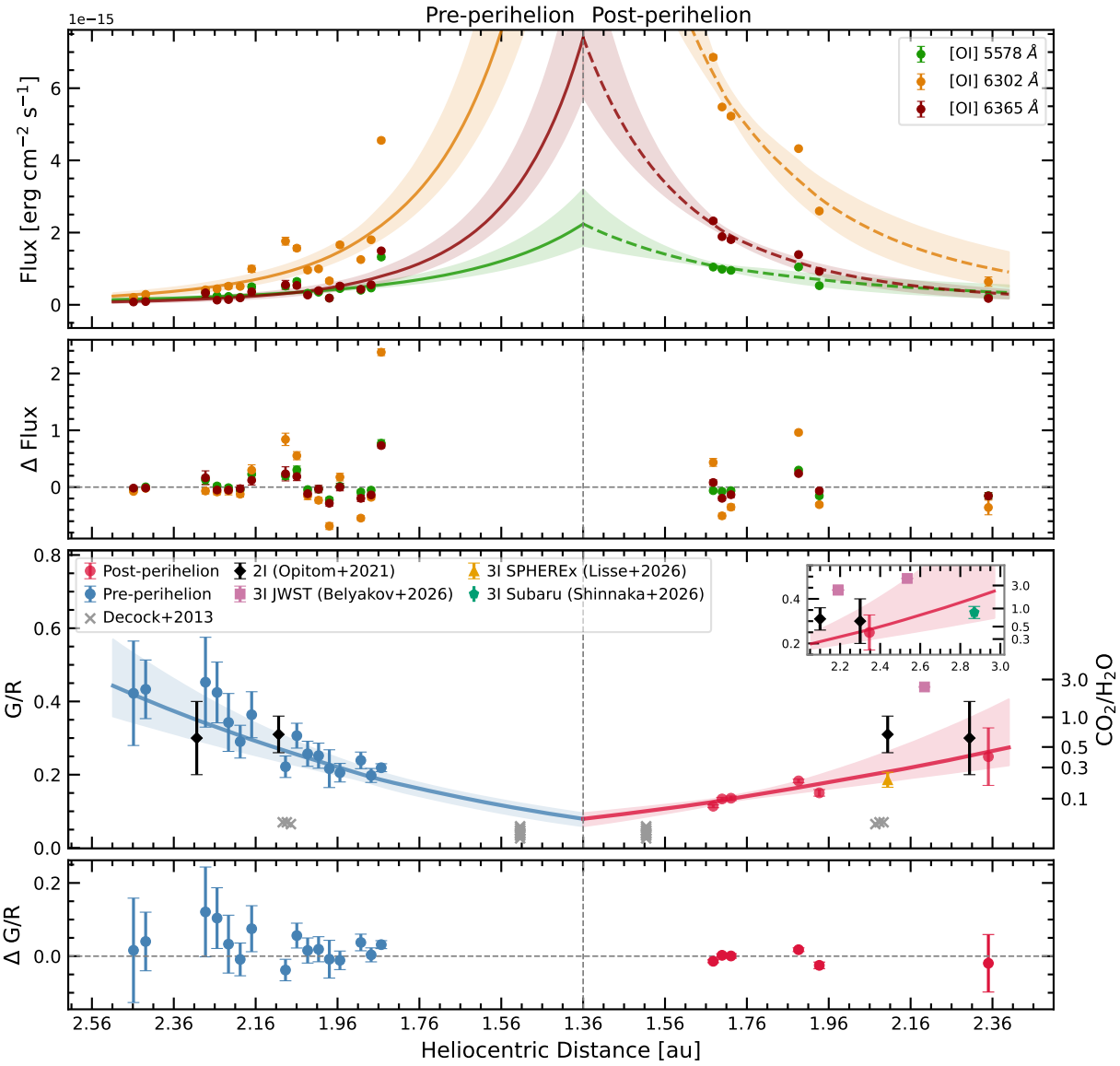

Fig. 8: 3I Oxygen forbidden line fluxes and the green-to-red ratio (G/R) as a function of heliocentric distance. *Top panel:* Individual [O I] line fluxes (5578 Å in green, 6302 Å in orange, and 6365 Å in dark red) with asymmetric power-law fits of the form $c(r_h/r_0)^a$, allowing independent slopes for the pre- and post-perihelion branches while enforcing continuity at perihelion (r_0 = 1.36 au). Solid lines show the pre-perihelion model and dashed lines show the post-perihelion model, each in the corresponding line color. Shaded regions indicate the 16th–84th percentile confidence bands. *Second panel:* Residuals of each line flux relative to its corresponding fit, color-coded as above. *Third panel:* G/R ratio, defined as the [O I] 5578 Å flux divided by the sum of the [O I] 6302 Å and 6365 Å fluxes. Our data are shown as colored circles (teal for pre-perihelion, crimson for post-perihelion). The G/R model solid curves and confidence bands are computed from the ratio of the individual line fits, with uncertainties propagated through the bootstrap resampling. The right y-axis shows the estimate of CO_2/H_2O using the Decock et al. (2013) prescription. The inset plot on the top right corresponds to an extension of the G/R fitted model to larger heliocentric distances, with the same axes. Gray crosses correspond to the comets 9P/Tempel 1 (Jupiter Family) and C/2009 P1 Garradd ($a > 10\,000$ au) from Decock et al. (2013) and black crosses to 2I/Borisov from Opitom et al. (2021), both of which are duplicated in the pre- and post-perihelion panels, the pink squares show measurements from Belyakov et al. (2026), the yellow triangle from Lisse et al. (2026), both corresponding to post-perihelion CO_2/H_2O measurements, the green pentagon shows the G/R ratio measured by Shinnaka et al. (2026). *Bottom panel:* Residuals of the G/R data relative to the derived model, with the same color coding. In all panels, the dashed gray vertical line marks perihelion and the horizontal dashed line in the residual panels shows the zero-residual value.

expect closer agreement between our values and JWST, since both use smaller apertures than SPHEREx (ours a circular aperture of radius 0.5″, JWST an annulus from 2–3″). One explanation is that the conversion from the G/R ratio to CO_2/H_2O depends on photodissociation rates that vary across the literature, that warrant further study, and are themselves functions of heliocentric distance and, potentially, solar activity. Different choices of photodissociation rates in the literature lead to a substantial spread in the derived ratios (e.g., Raghuram & Bhardwaj 2013; McKay et al. 2016; Kawakita 2022). We, therefore, em-

phasize that our [O I]-based CO_2/H_2O values are indirect proxies, and that direct infrared measurements should be preferred where available. Nevertheless, the overall picture of a decreasing CO_2/H_2O ratio with heliocentric distance and its elevated values remains consistent within the framework of our analysis. Other, physical explanations for a water excess in the JWST measurements are also possible: the JWST annulus may still be insufficient to avoid the optically thick regime of H_2O, or the dominant water source may transition at those distances (1.9 – 2.4 au) from sublimating icy grains to the nucleus surface (Combi et al. 2013; Bodewits et al. 2014). However, we emphasize that only one of the JWST ratios is inconsistent, which is not enough to clearly establish the cause.

As an internal consistency check, we examine the red doublet ratio F_{6302}/F_{6365}, whose theoretical value is set by the branching ratio of the $O(^1D) \rightarrow O(^3P)$ transition, i.e., 3.096 in the non-relativistic calculation of Galavis et al. (1997), and 2.997 when relativistic corrections are included (Storey & Zeippen 2000). From the per-night line intensities listed in Table E.2, nearly all measured ratios are consistent with the Storey & Zeippen (2000) value within 1σ, and all but one within 2σ. The sole outlier is night E3, where the 6365 Å line is severely blended with a nearby telluric feature and affected by low S/N. The weighted mean of all nights yields $F_{6302}/F_{6365} = 2.97 \pm 0.03$.

6. Conclusions

The arrival of 3I/ATLAS, the third known interstellar object to traverse the Solar System, provides a rare opportunity to probe the chemistry of another planetary system using the full arsenal of solar-system observational tools. We have monitored 3I/ATLAS with the high-resolution spectrograph ESPRESSO ($R \simeq 140\,000$) on the ESO 8.2 m VLT across both branches of its perihelion passage, with pre-perihelion observations starting in early September 2025 and post-perihelion observations until late November–December 2025, spanning $r_h = 1.67$–2.45 au (Table E.1). The data were reduced with the standard ESPRESSO pipeline and analyzed with our publicly released Python package CometSpec, which we developed to perform fluorescence modeling of the CN violet band (including the Swings effect, rotational/collisional coupling, and a flexible LSF) together with MCMC fitting, and Voigt-profile decomposition of the forbidden [O I] lines. From these fits we derive CN production rates and the oxygen green-to-red ratio across the full campaign. In addition we construct a fluorescence model for C_2 and Fe plus the line fitting of CH. Our main results are as follows.

- CN production rate evolution. We detect CN on 18 of 22 useful observed nights, with 50%-completeness upper limits on the remaining four epochs. The pre-perihelion heliocentric evolution is well described by a power law $Q_{CN} \propto r_h^b$ with $b_{pre} = -4.62^{+1.25}_{-1.22}$, within the range observed for solar-system comets (A'Hearn et al. 1995). The post-perihelion sampling is too sparse to establish an asymmetric pre/post evolution at high confidence. The data are consistent with both a single-branch power law and a piecewise-asymmetric model. The residual scatter about the smooth model exceeds the formal uncertainties and is plausibly driven by a combination of atmospheric, comet-centering, and Haser-model systematics plus physical effects (rotation, outbursts, solar-wind variability) that the present cadence cannot separate. The comparison with Cordiner et al. (2026) is consistent with HCN being the dominant parent of CN; however, other HCN measurements are inconsistent with this interpretation.
- Forbidden oxygen lines. The three forbidden [O I] lines at 5578, 6302, and 6365 Å are detected at high signal-to-noise on nearly every night. The measured red-doublet flux ratio, $F_{6302}/F_{6365} = 2.97 \pm 0.03$, agrees with the relativistic theoretical value of Storey & Zeippen (2000), providing an independent confirmation of our flux calibration and the absence of significant line blending (with the sole exception of epoch E3, where the 6365 Å line suffers from a strong telluric blend at low S/N).
- G/R ratio and CO_2/H_2O proxy. The green-to-red ratio declines steadily from $\sim 0.42 \pm 0.14$ at $r_h \simeq 2.4$ au to $\sim 0.114 \pm 0.004$ near perihelion. The asymmetric piecewise model is strongly preferred over the symmetric fit (ΔBIC = 105, 2011, 277 for the 5578, 6302, and 6365 Å lines, respectively), with the post-perihelion branch declining more gradually than the pre-perihelion one, as expected from the delayed H_2O sublimation predicted by thermal-inertia models. Our G/R values are elevated relative to solar-system Oort-Cloud and Jupiter-family comets and are comparable to those measured for 2I/Borisov, placing both interstellar visitors above the locus of solar-system comets in the G/R–r_h plane; however, for this study the small aperture can affect the comparison. Translated via the Decock et al. (2013) prescription, the inferred CO_2/H_2O proxy spans ~ 0.06 near perihelion to ~ 1.06 at $r_h \gtrsim 2$ au, consistent with the trends reported from Subaru/HDS, SPHEREx, and JWST, and supporting a picture in which 3I/ATLAS hosts an exceptionally CO_2-rich coma that becomes progressively H_2O-dominated near perihelion. Denser sampling across future interstellar cometary perihelion passages will be needed to establish this asymmetry at the level of individual solar-system comets.
- Emission-line inventory. Beyond CN and [O I], we identify Ni I and Fe I emission on multiple nights (Sect. 4.6), and detect C_2 Swan and CH (4300 Å) bands more clearly in the post-perihelion stack than in the pre-perihelion data. From the first three post-perihelion nights we derive $\log Q_{C_2}$ in the range [25.20, 25.68] and $\log Q_{CH} = 26.38 \pm 0.05$, corresponding to $\log Q_{C_2}/Q_{CN} \in [-0.79, -0.10]$ and $\log Q_{CH}/Q_{CN} = 0.31 \pm 0.12$. These ratios place 3I/ATLAS near the boundary of the carbon-chain-depleted class (A'Hearn et al. 1995), broadly consistent with the pre-perihelion classifications of Rahatgaonkar et al. (2025), Salazar Manzano et al. (2025), Lazzarin et al. (2026), and Hutsemékers et al. (2026). A direct comparison of Fe I production rates between two nights at nearly identical heliocentric distances (E17 at 1.85 au and E21 at 1.88 au) yields $\log Q_{Fe} = 24.42 \pm 0.06$ and 24.41 ± 0.08, respectively, i.e., no detectable pre/post-perihelion asymmetry. A larger matched-r_h sample, tracking iron emission from its onset to its shut-off, would test the thermal models of iron-bearing carbonyl carriers (Hutsemékers et al. 2026) and the heliocentric thermal asymmetry inherent to such a scenario (Manfroid et al. 2021; Rahatgaonkar et al. 2025).

7. Data availability

To enable independent reanalysis and comparison, and to facilitate the community follow-up that the next interstellar visitor will require, CometSpec is publicly available on GitHub at https://github.com/baltasarluco/CometSpec; and the reduced 1D spectra (per-night and combined stacks), derived continuum models, corner plots, and fit plots are released on Zenodo at https://zenodo.org/records/20966879.

Acknowledgements. We are grateful to the ESO Garching and Paranal observatory staff for their extraordinary support during the implementation and ex-

ecution of the observations, in particular we thank Martina Baratella, Susana Cerda-Hernandez, Claudia Cid, Enrico Congiu, Alex Correa, Robert De Rosa, Julien Drevon, Lorena Faundez, Abigail Frost, Javier Fuentes, Elisa Garro, Boris Haeussler, Ana Jimenez Gallardo, Aaron Labdon, Francesca Lucertini, John Pritchard, and Jose Velasquez. We thank Dennis Bodewits for valuable discussions and comments on the manuscript, and the referee, John Noonan, for a constructive report that improved this work. We acknowledge support from the Chilean National Agency for Research and Development (ANID) in form of the grant CATA-Basal FB210003 and the Beca de Doctorado Nacional (RR, JPC). This research has made use of data and/or services provided by the International Astronomical Union's Minor Planet Center, the NASA's Jet Propulsion Laboratory's Horizons System, and the NASA/IPAC Extragalactic Database, which is funded by the National Aeronautics and Space Administration and operated by the California Institute of Technology.
This work is dedicated to the memory of Vicente Maximiliano Gebauer Molina.

References

A'Hearn, M. F., Millis, R. C., Schleicher, D. O., Osip, D. J., & Birch, P. V. 1995, Icarus, 118, 223
Bannister, M. T., Opitom, C., Fitzsimmons, A., et al. 2020, arXiv e-prints, arXiv:2001.11605
Belyakov, M., Wong, I., Bolin, B. T., et al. 2026, ApJ, 1001, L11
Bhardwaj, A. & Haider, S. A. 2002, Advances in Space Research, 29, 745
Bhardwaj, A. & Raghuram, S. 2012, ApJ, 748, 13
Biver, N., Bockelée-Morvan, D., Moreno, R., et al. 2026, A&A, 708, L16
Bockelée-Morvan, D., Calmonte, U., Charnley, S., et al. 2015, Space Sci. Rev., 197, 47
Bodewits, D., Farnham, T. L., A'Hearn, M. F., et al. 2014, ApJ, 786, 48
Bodewits, D., Noonan, J. W., Feldman, P. D., et al. 2020, Nature Astronomy, 4, 867
Borisov, G. & Minor Planet Center. 2019, MPEC 2019-R106: COMET C/2019 Q4 (Borisov), Minor Planet Electronic Circular
Bromley, S. J., Neff, B., Loch, S. D., et al. 2021, Planet. Sci. J., 2, 228
Bromley, S. J., Noonan, J. W., Cochran, A. L., et al. 2024, MNRAS, 528, 7358
Brooke, J. S. A., Ram, R. S., Western, C. M., et al. 2014, ApJS, 210, 23
Cambianica, P., Cremonese, G., Munaretto, G., et al. 2021, A&A, 656, A160
Cochran, A. L., Barker, E. S., & Gray, C. L. 2012, Icarus, 218, 144
Cochran, A. L. & Schleicher, D. G. 1993, Icarus, 105, 235
Combi, M. R. & Delsemme, A. H. 1980, ApJ, 237, 641
Combi, M. R., Mäkinen, J. T. T., Bertaux, J.-L., et al. 2013, Icarus, 225, 740
Combi, M. R. & McCrosky, R. E. 1991, Icarus, 91, 270
Cordiner, M. A., Milam, S. N., Biver, N., et al. 2020, Nature Astronomy, 4, 861
Cordiner, M. A., Roth, N. X., Kelley, M. S. P., et al. 2025, ApJ, 991, L43
Cordiner, M. A., Roth, N. X., Micheli, M., et al. 2026, arXiv e-prints, arXiv:2603.06911
Coulson, I. M., Kuan, Y.-J., Charnley, S. B., et al. 2026, MNRAS, 546, stag063
de la Fuente Marcos, R., Alarcon, M. R., Licandro, J., et al. 2025, A&A, 700, L9
Decock, A., Jehin, E., Hutsemékers, D., & Manfroid, J. 2013, A&A, 555, A34
Decock, A., Jehin, E., Rousselot, P., et al. 2015, A&A, 573, A1
Denneau, L., Siverd, R., Tonry, J., et al. 2025, Minor Planet Electronic Circulars, 2025-N12
Festou, M. & Feldman, P. D. 1981, A&A, 103, 154
Fink, U. & Johnson, J. R. 1984, AJ, 89, 1565
Fitzsimmons, A., Hainaut, O., Meech, K. J., et al. 2019, ApJ, 885, L9
Fitzsimmons, A., Snodgrass, C., Rozitis, B., et al. 2018, Nature Astronomy, 2, 133
Foreman-Mackey, D., Hogg, D. W., Lang, D., & Goodman, J. 2013, PASP, 125, 306
Fray, N., Bénilan, Y., Cottin, H., Gazeau, M.-C., & Crovisier, J. 2005, Planet. Space Sci., 53, 1243
Freudling, W., Romaniello, M., Bramich, D. M., et al. 2013, A&A, 559, A96
Füri, E. & Marty, B. 2015, Nature Geoscience, 8, 515
Galavis, M. E., Mendoza, C., & Zeippen, C. J. 1997, A&AS, 123, 159
Götz, C., Deca, J., Mandt, K., & Volwerk, M. 2024, in Comets III, ed. K. J. Meech, M. R. Combi, D. Bockelée-Morvan, S. N. Raymond, & M. E. Zolensky, 543–574
Hall, L. A. & Anderson, G. P. 1991, J. Geophys. Res., 96, 12,927
Hanuschik, R. W. 2003, A&A, 407, 1157
Haser, L. 1957, Bulletin de la Societe Royale des Sciences de Liege, 43, 740
Hopkins, M. J., Dorsey, R. C., Forbes, J. C., et al. 2025, ApJ, 990, L30
Huebner, W. F. & Mukherjee, J. 2015, Planet. Space Sci., 106, 11
Hutsemékers, D., Manfroid, J., Jehin, E., Opitom, C., & Moulane, Y. 2021, A&A, 652, L1
Hutsemékers, D., Manfroid, J., Jehin, E., et al. 2026, A&A, 706, A43
Jewitt, D. 2003, Earth Moon and Planets, 92, 465
Kawakita, H. 2022, ApJ, 931, 24
Kawakita, H., Tsujimoto, K., Shinnaka, Y., et al. 2026, ApJ, 1000, L60
Kawakita, H., Watanabe, J.-i., Furusho, R., et al. 2004, ApJ, 601, 1152
Knight, M. M. & Schleicher, D. G. 2013, Icarus, 222, 691
Kramida, A., Yu. Ralchenko, Reader, J., & and NIST ASD Team. 2024, NIST Atomic Spectra Database (ver. 5.12), [Online]. Available: https://physics.nist.gov/asd [2016, January 31]. National Institute of Standards and Technology, Gaithersburg, MD.
Kurucz, R. L. 2005, Mem. Soc. Astron. Italiana Suppl., 8, 189
Lazzarin, M., Mura, A. C., La Forgia, F., et al. 2026, ApJ, 998, L30
Lin, H. W., Lee, C.-H., Gerdes, D. W., et al. 2020, ApJ, 889, L30
Lisse, C. M., Bach, Y. P., Bryan, S., et al. 2025, RNAAS, 9, 242
Lisse, C. M., Bach, Y. P., Bryan, S. A., et al. 2026, RNAAS, 10, 26
Magnani, L. & A'Hearn, M. F. 1986, ApJ, 302, 477
Manfroid, J., Hutsemékers, D., & Jehin, E. 2021, Nature, 593, 372
Manfroid, J., Jehin, E., Hutsemékers, D., et al. 2009, A&A, 503, 613
McGlynn, T. A. & Chapman, R. D. 1989, ApJ, 346, L105
McKay, A. J., Chanover, N. J., Morgenthaler, J. P., et al. 2013, Icarus, 222, 684
McKay, A. J., Cochran, A. L., Dello Russo, N., & DiSanti, M. A. 2020, ApJ, 889, L10
McKay, A. J., Cochran, A. L., DiSanti, M. A., et al. 2015, Icarus, 250, 504
McKay, A. J., Kelley, M. S. P., Cochran, A. L., et al. 2016, Icarus, 266, 249
McKemmish, L. K., Syme, A.-M., Borsovszky, J., et al. 2020, MNRAS, 497, 1081
Meech, K. J., Weryk, R., Micheli, M., et al. 2017, Nature, 552, 378
Micheli, M., Farnocchia, D., Meech, K. J., et al. 2018, Nature, 559, 223
Mommert, M., Kelley, M., de Val-Borro, M., et al. 2019, The Journal of Open Source Software, 4, 1426
Moulane, Y., Jehin, E., Manfroid, J., et al. 2023, A&A, 670, A159
Noonan, J. W., Stern, S. A., Feldman, P. D., et al. 2018, AJ, 156, 16
Opitom, C., Jehin, E., Hutsemékers, D., et al. 2021, A&A, 650, L19
Opitom, C., Snodgrass, C., Jehin, E., et al. 2025, MNRAS, 544, L31
'Oumuamua ISSI Team, Bannister, M. T., Bhandare, A., et al. 2019, Nature Astronomy, 3, 594
Pepe, F., Cristiani, S., Rebolo, R., et al. 2021, A&A, 645, A96
Persson, S. E. 2022, PASP, 134, 075001
Pierce, D. M. & Cochran, A. L. 2021, Planet. Sci. J., 2, 19
Puzia, T. H., Rahatgaonkar, R., Carvajal, J. P., Nayak, P. K., & Luco, B. 2025, ApJ, 990, L27
Raghuram, S. & Bhardwaj, A. 2013, Icarus, 223, 91
Raghuram, S. & Bhardwaj, A. 2014, A&A, 566, A134
Rahatgaonkar, R., Carvajal, J. P., Puzia, T. H., et al. 2025, ApJ, 995, L34
Romano, D. 2022, A&A Rev., 30, 7
Roth, N. X., Cordiner, M. A., Bockelée-Morvan, D., et al. 2026, ApJ, 999, L32
Rousselot, P., Hill, S. M., Burger, M. H., et al. 2000, Icarus, 146, 263
Salazar Manzano, L. E., Lin, H. W., Taylor, A. G., et al. 2025, ApJ, 993, L23
Santana-Ros, T., Ivanova, O., Mykhailova, S., et al. 2025, A&A, 702, L3
Schleicher, D. G., Millis, R. L., Osip, D. J., & Birch, P. V. 1991, Icarus, 94, 511
Schleicher, D. G., Millis, R. L., Thompson, D. T., et al. 1990, AJ, 100, 896
Seligman, D. Z., Micheli, M., Farnocchia, D., et al. 2025, ApJ, 989, L36
Serra-Ricart, M., Licandro, J., & Alarcon, M. R. 2026, A&A, 705, L3
Shinnaka, Y., Tsujimoto, K., Kawakita, H., et al. 2026, AJ, 171, 281
Slanger, T. G., Cosby, P. C., Sharpee, B. D., Minschwaner, K. R., & Siskind, D. E. 2006, Journal of Geophysical Research (Space Physics), 111, A12318
Sneden, C., Lucatello, S., Ram, R. S., Brooke, J. S. A., & Bernath, P. 2014, ApJS, 214, 26
Storey, P. J. & Zeippen, C. J. 2000, MNRAS, 312, 813
Tonry, J. L., Denneau, L., Heinze, A. N., et al. 2018, PASP, 130, 064505
van Hoof, P. A. M. 2018, Galaxies, 6, 63
Xing, Z., Bodewits, D., Noonan, J., & Bannister, M. T. 2020, ApJ, 893, L48
Yaginuma, A., Taylor, A. G., & Seligman, D. Z. 2026, MNRAS, 546, stag162
Ye, Q.-Z., Zhang, Q., Kelley, M. S. P., & Brown, P. G. 2017, ApJ, 851, L5
Yurchenko, S. N., Szabó, I., Pyatenko, E., & Tennyson, J. 2018, MNRAS, 480, 3397

Appendix A: CometSpec – a flexible radiative fluorescence model package

CometSpec fits the radiative fluorescence model to the spectroscopic data via MCMC using the affine-invariant ensemble sampler implemented in emcee (Foreman-Mackey et al. 2013). The user can choose which parameters are left free among the column density $\log N$ (of one or more isotopologues), the LSF parameters (e.g., Gaussian or Lorentzian widths), $f_{\rm col}$, and $T_{\rm kin}$. Any of these can also be held fixed.

The first 50% of each chain is discarded as burn-in. After convergence, CometSpec optionally applies an iterative filter to the remaining posterior samples, retaining only those whose log-probability lies within a given threshold of the maximum log-probability reached by the sampler. The threshold starts at 5σ and is reduced at each iteration until the absolute difference between the mean and the median of the surviving chain becomes smaller than 10% of the median value, thereby isolating the high-probability core of the posterior around the global maximum. This step can be disabled via a runtime flag.

Best-fit values are reported as the median of the retained chain, and the associated uncertainties as the mean of the $|\text{median} - 16^{\text{th}}|$ and $|84^{\text{th}} - \text{median}|$ percentile differences. When the iterative filter is enabled, the reported uncertainties describe the dispersion within the high-probability core and are, therefore, smaller than those derived from the full posterior. This reflects our interpretation that samples with substantially lower log-probability are treated as outliers relative to the dominant solution. The procedure yields robust best-fit values and uncertainties even when the posterior exhibits multiple converged regions, an example is shown in Fig. A.1.

The iterative filter is meaningful only when the lines are clearly detected and the parameter space is well sampled around a true maximum. For non-detections, where the chain does not converge to a well-defined peak, filtering around the maximum log-probability is ill-defined, and we instead report uncertainties from the full posterior.

Appendix B: Isotopologue search

To search for isotopologues, we used the night of December 25 and the stack of the first three post-perihelion nights. We did not include additional nights in the stack, as the signal-to-noise ratio decreases owing to the exponential decline of the CN emission. Adopting the fitted ^{12}C^{14}N model from December 25 as a prior, we constructed models for ^{13}C^{14}N and ^{12}C^{15}N at their expected line positions. We then stacked these lines weighted by their predicted relative intensities, so that the expected stronger lines contribute more. Neither the December 25 night nor the stacked spectrum yielded a detection of any isotopologue.

Appendix C: Fe, C_2 and CH

We use CometSpec to fit fluorescence models of Fe, C_2, and we compute CH production rates from line fluxes.

Iron. For Fe, we adopt the line list of van Hoof (2018). We retrieved all transitions in the 2 000–10 000 Å range and retained those with $A_{ul} > 10^3\,\mathrm{s}^{-1}$ and upper-level energies below 40 000 cm^{-1}, following Manfroid et al. (2021) line filtering, with some modifications, for instance we did not apply lower-level filters and our wavelength range of lines included is different. The solar irradiance was extended into the UV using the Hall & Anderson (1991) spectrum over 2 000–2 990 Å. We then performed independent fits in successive 100 Å-wide windows, with the MCMC simultaneously sampling a Lorentzian LSF width, a line velocity shift, and $\log N$ (10 walkers, 1 000 steps, i.e., 3×10^4 iterations per window). The Fe production rate was derived assuming a column-density profile $N(\rho) \propto \rho^{-1}$, where ρ is the projected comet-centric distance (Manfroid et al. 2021). Per-window uncertainties were estimated as for CN, combining statistical and slit-loss contributions and adopting the mean of the upper and lower $\log N$ errors. A single per-night $\log Q_{\rm Fe}$ was then obtained as the variance-weighted mean across windows, with Gaussian error propagation. We measure $\log Q_{\rm Fe} = 24.42 \pm 0.06$ on 2025 September 24 and 24.41 ± 0.08 on 2025 December 4.

C_2. For C_2, the default line list is the recommended ExoMol[11] compilation (Yurchenko et al. 2018; McKemmish et al. 2020). We applied the following selection criteria: wavelengths in the range 3 000–10 000 Å, upper-level energies $< 30\,000\,\mathrm{cm}^{-1}$, $A_{ul} > 2 \times 10^6\,\mathrm{s}^{-1}$, vibrational quantum number $v < 5$, rotational quantum number $N < 50$, and only the $a\,^1\Pi_u - x\,^1\Sigma_g^+$, $b\,^3\Sigma_g^- - a\,^3\Pi_u$, $d\,^3\Pi_g - a\,^3\Pi_u$, $d\,^3\Pi_g - c\,^3\Sigma_u^+$, $a\,^3\Pi_u - x\,^1\Sigma_g^+$, and $c\,^3\Sigma_u^+ - x\,^1\Sigma_g^+$ transitions. The last three conditions are adopted from Rousselot et al. (2000) but with more restrictive thresholds. We note that the number of transitions increases substantially if the A_{ul} criterion is relaxed.

The fluorescence modeling follows the same scheme as for CN, except that the collisional selection rules depend on the isotopologue. For $^{12}C_2$, only $|\Delta J| = 2$ transitions are allowed, since it is homonuclear with nuclear spin 0; for $^{13}C_2$, $|\Delta J| = 0, 2$ transitions are permitted, as it is homonuclear with nuclear spin 1/2 and exhibits ortho–para separation; and for ^{12}C ^{13}C, all $|\Delta J| = 0, 1, 2$ transitions are allowed, since it is heteronuclear. In all cases, collisions are restricted to transitions from upper levels to the lowest state in the line list (or vice versa). It is important to highlight that collisions for this model are more complicated, with significant degeneracy among the parameters.

For $^{12}C_2$ we fitted only the column density $\log N$, the LSF FWHM, and a velocity shift. The kinetic temperature was fixed at $T_{\rm kin} = 100$ K, and we ran three independent fits, with $f_{\rm col} = -3.12$, $f_{\rm col} = 8.52$, and no collisions, in order to bracket the impact of collisional thermalization, Fig. C.1 shows the no-collision fit. These choices reflect both the high computational cost of the full model and the strong parameter degeneracies inherent to fitting a single band at low signal-to-noise. Each chain used 10 walkers and 500 steps. We fitted the stacked spectrum of the first three post-perihelion nights, with the solar irradiance scaled to the mean heliocentric distance of those epochs. Adopting the parent scale length of 2.2×10^4 km and daughter scale length of 6.6×10^4 km, both scaled by r^{-2} (A'Hearn et al. 1995) and the same outflow velocity as for CN, we obtain $\log Q_{C_2} \in [25.20, 25.68]$ across the three fits, corresponding to $\log(Q_{C_2}/Q_{CN}) \in [-0.79, -0.10]$ when compared to the mean CN production rate over the same epochs (E18, E19 and E20). The systematic uncertainty associated with the parameter degeneracies is likely underestimated by these formal ranges.

CH. For CH, the short radiative lifetime makes a full fluorescence treatment impractical, and we instead estimate the production rate from a direct flux measurement. We fitted the

[11] https://www.exomol.com/data/molecules/C2/

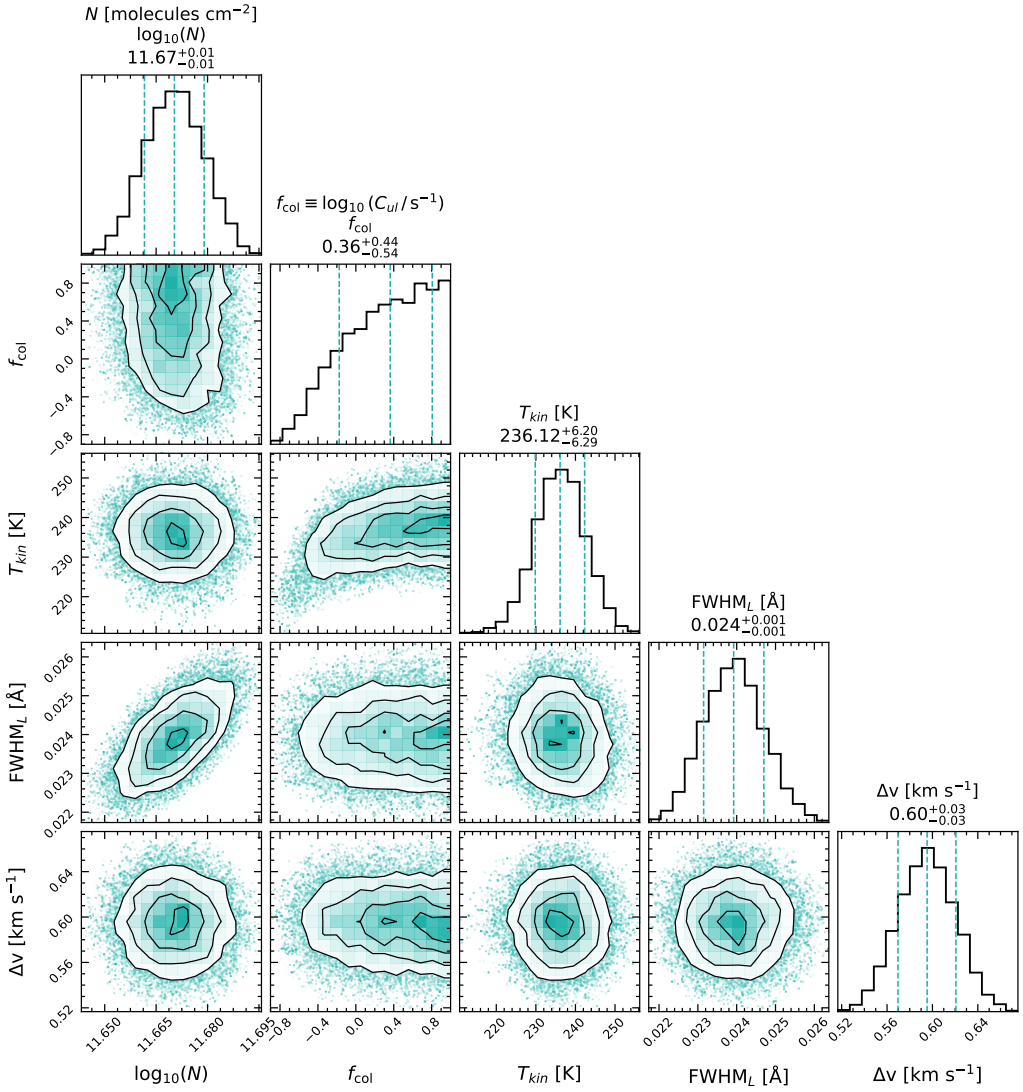

Fig. A.1: MCMC parameter fits for the spectrum, fitting the parameters as described in Sect. 4.2. Black contours indicate the 16th, 50th, and 84th percentiles, which are also marked as dashed cyan lines in the marginalized histograms.

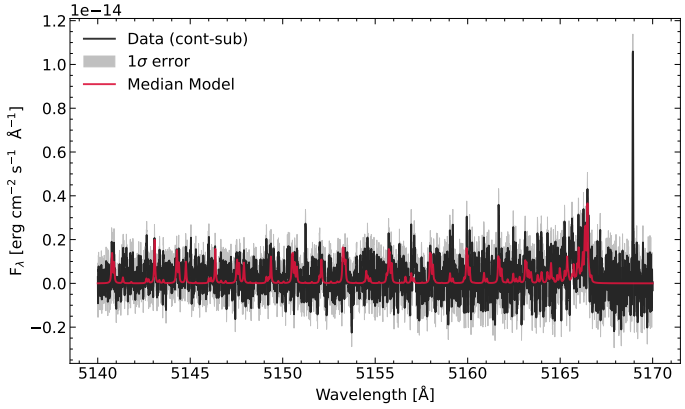

Fig. C.1: C_2 fluorescence fit for the stacked spectrum of the first three post-perihelion nights. The black line shows the data with their 1 σ uncertainties; the red line is the non-collisional fluorescence fit. The prominent line at 5169 Å corresponds to a Fe line.

CH lines in the stack of the first three post-perihelion nights, summed their fluxes, converted them to column densities using Table 2 of Cochran et al. (2012), and applied a Haser model with the parent scale length of 7.8×10^4 km and the daughter scale length 4.8×10^3 km both scaled by r^{-2} and from the same reference. Including the slit-loss contribution, we obtain $\log Q_{CH} = 26.38 \pm 0.05$ and $\log(Q_{CH}/Q_{CN}) = 0.31 \pm 0.12$ when compared to the mean CN production rate of the same three nights (E18, E19 and E20).

Appendix D: Continuum evolution

We studied the continuum evolution throughout our observations to assess the scatter present in the data. For this purpose, we computed the variance-weighted mean of the flux density in the window 6071–6076 Å, chosen because it is relatively free of sky emission lines, telluric absorption, and solar continuum absorption. The slit-loss error was added in quadrature to the flux error, and the same fitting procedure applied to the CN evolution was then used. The resulting fit, shown in Fig. D.1, reveals a large scatter that points toward a systematic origin. As with CN, the asymmetric profile is preferred over the symmetric one, with ΔBIC = 60.7, and the fit parameters are listed in Table D.1. It is

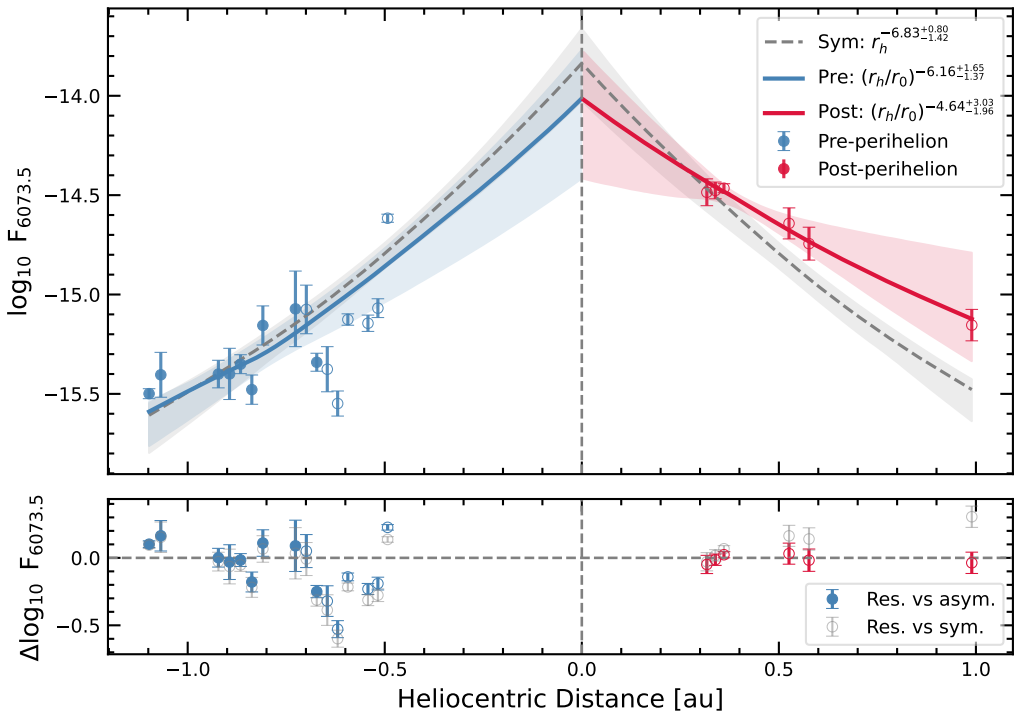

Fig. D.1: Continuum evolution of 3I at different heliocentric distances. *Upper panel:* Continuum flux in the 6071–6076 Å window (logarithmic scale) as a function of heliocentric distance $r_{\rm h}$. Blue and red symbols denote pre- and post-perihelion measurements, with 1σ error bars; the vertical dashed line marks perihelion. The black dashed line and gray band show the symmetric fit $F_{6073.5} = a\, r_{\rm h}^{b}$ and its 1σ confidence region; the blue and red curves show the asymmetric piecewise fit, continuous at perihelion. Open and filled symbols indicate nights without and with sky subtraction, respectively. *Lower panel:* Residuals with respect to the asymmetric fit (color-coded as above) and to the symmetric fit (open gray symbols); the horizontal dashed line marks zero. Colored symbol styles follow the convention of the upper panel.

important to emphasize that the lack of sky subtraction on some nights did not affect the CN analysis, since the continuum was fitted independently; however, its contribution must be taken into account when interpreting Fig. D.1.

Table D.1: Continuum fits of the heliocentric scaling relation $F_{\rm cont} = a\,(r_{\rm h}/1\ {\rm au})^{b}$ and $F_{\rm cont} = F_{\rm peri}\,(r_{\rm h}/r_0)^{b}$

Data included	$\log a$	b	$\log F_{\rm peri}$
Both	$-12.93^{+0.36}_{-0.29}$	$-6.83^{+0.80}_{-1.42}$	—
Pre	—	$-6.16^{+1.65}_{-1.37}$	$-14.01^{+0.24}_{-0.40}$
Post	—	$-4.64^{+3.03}_{-1.96}$	$-14.01^{+0.24}_{-0.40}$

Appendix E: Tables

Table E.1: Journal of 3I observations with VLT/ESPRESSO.

Visit[a]	Date (UT)	Target	Exp. Time (s)	Airmass[b]	Seeing[c] (″)	r_h[d] (au)	$\dot{r}$[d] (km s^{-1})	Δ[e] (au)	$\dot{\Delta}$[e] (km s^{-1})
⋆E1-1	2025-09-02 23:37–02:19	3I/ATLAS	9 × 600	1.26 – 2.08	0.40 – 0.53	2.45	−51.56	2.57	−4.51
		Sky	2 × 600	—	—	—	—	—	—
		HD 150469	1 × 600	—	—	—	—	—	—
⋆E2-1	2025-09-03 23:24–02:04	3I/ATLAS	12 × 600	1.22 – 2.64	0.44 – 0.82	2.42	−51.30	2.57	−4.28
		Sky	2 × 300	—	—	—	—	—	—
⋆E3-2	2025-09-08 00:26–01:13	3I/ATLAS	3 × 600	1.81 – 2.09	0.98 – 1.12	2.28	−49.85	2.55	−3.47
		Sky	1 × 300	—	—	—	—	—	—
⋆E4-1[f]	2025-09-09 23:34–01:17	3I/ATLAS	7 × 600	1.48 – 2.45	0.92 – 1.10	2.25	−49.53	2.55	−3.40
		Sky	1 × 300	—	—	—	—	—	—
⋆E5-1	2025-09-10 23:33–00:22	3I/ATLAS	3 × 600	1.50 – 1.66	0.74 – 0.88	2.22	−49.20	2.55	−3.35
		Sky	1 × 300	—	—	—	—	—	—
⋆E6-1	2025-09-11 23:27–01:01	3I/ATLAS	6 × 600	1.49 – 2.19	0.68 – 0.82	2.19	−48.84	2.55	−3.28
		Sky	2 × 300	—	—	—	—	—	—
⋆E7-2	2025-09-12 23:41–00:33	3I/ATLAS	3 × 600	1.66 – 1.88	0.60 – 0.99	2.17	−48.47	2.55	−3.24
		Sky	1 × 300	—	—	—	—	—	—
⋆E8-2	2025-09-15 23:21–00:26	3I/ATLAS	4 × 600	1.64 – 2.04	0.78 – 1.40	2.08	−47.25	2.54	−3.27
		Sky	1 × 300	—	—	—	—	—	—
E9-2	2025-09-16 23:49–00:42	3I/ATLAS	4 × 600	1.98 – 2.64	0.94 – 1.18	2.06	−46.81	2.54	−3.30
⋆E10-1	2025-09-17 23:26–00:28	3I/ATLAS	4 × 600	1.75 – 2.26	0.74 – 0.78	2.03	−46.36	2.54	−3.38
		Sky	4 × 300	—	—	—	—	—	—
E11-1	2025-09-18 23:11–00:33	3I/ATLAS	6 × 600	1.74 – 2.74	0.71 – 0.90	2.00	−45.88	2.53	−3.46
E12-1	2025-09-19 23:35–00:11	3I/ATLAS	3 × 600	2.01 – 2.37	0.86 – 0.94	1.98	−45.38	2.53	−3.57
E13-1	2025-09-20 23:21–23:47	3I/ATLAS	3 × 600	1.92 – 2.29	0.58 – 0.64	1.95	−44.86	2.53	−3.70
E14-1[g]	2025-09-21 23:02–23:48	3I/ATLAS	2 × 600	1.88 – 2.24	0.71 – 0.89	1.93	−44.32	2.53	−3.84
E15-1	2025-09-22 23:17–23:53	3I/ATLAS	3 × 600	2.02 – 2.37	0.63 – 0.72	1.90	−43.75	2.52	−4.00
E16-1	2025-09-23 23:22–23:58	3I/ATLAS	3 × 600	2.18 – 2.62	0.66 – 0.75	1.87	−43.15	2.52	−4.17
E17-2	2025-09-24 23:10–23:56	3I/ATLAS	3 × 600	2.26 – 2.73	0.48 – 0.53	1.85	−42.53	2.52	−4.37
E18-2	2025-11-25 08:20–08:56	3I/ATLAS	3 × 600	2.07 – 2.44	0.63 – 0.79	1.67	36.81	1.98	−21.67
E19-3	2025-11-26 08:21–09:02	3I/ATLAS	3 × 600	1.91 – 2.21	0.40 – 0.64	1.70	37.67	1.97	−21.33
E20-2	2025-11-27 08:26–09:03	3I/ATLAS	6 × 600	1.82 – 2.08	0.55 – 0.62	1.72	38.48	1.95	−20.96
E21-3	2025-12-04 07:22–08:35	3I/ATLAS	6 × 600	1.64 – 2.35	0.64 – 0.80	1.88	43.35	1.88	−17.03
E22-3[h]	2025-12-06 07:29–08:26	3I/ATLAS	6 × 600	1.61 – 2.10	0.78 – 0.95	1.93	44.50	1.86	−15.44
E23-1	2025-12-21 05:47–07:18	3I/ATLAS	7 × 600	1.41 – 1.87	0.54 – 0.86	2.35	50.56	1.80	2.82

Notes. [a] Observing visit identifiers for ESPRESSO, E + epoch number - UT telescope number, nights with sky subtraction start with a ⋆ symbol. Each entry corresponds to a distinct observing night, including comet and if applicable solar analog and/or sky exposures. [b] Airmass range of the target during the science exposures. [c] DIMM seeing values from Paranal ambient telemetry during the science exposures. [d] Mean heliocentric distance and velocity of the target during science exposures (JPL Horizons). [e] Mean geocentric distance and velocity of the target during science exposures (JPL Horizons). [f] Due to star contamination, one exposure was discarded. [g] Due to technical problems, compromised-quality data were taken during the night. [h] Due to bad weather conditions the first exposure was discarded.

Table E.2: 3I Fit results

Visit	log Q_{CN}/(molecules s^{-1})	Oxygen Flux (10^{-16} erg cm^{-2} s^{-1})			G/R	CO_2/H_2O [a]	Fitted $\dot{\Delta}$ (km s^{-1})		
		5578 Å	6302 Å	6365 Å			5578 Å	6302 Å	6365 Å
E1	≤ 25.39	1.21 ± 0.40	2.06 ± 0.21	0.79 ± 0.33	0.42 ± 0.14	–	−3.84 ± 0.63	−4.53 ± 0.13	−4.22 ± 0.85
E2	≤ 25.55	1.67 ± 0.24	2.87 ± 0.23	0.90 ± 0.33	0.43 ± 0.08	–	−3.90 ± 0.24	−4.47 ± 0.11	−4.40 ± 0.72
E3	≤ 25.95	3.42 ± 0.76	4.14 ± 0.52	3.30 ± 1.22	0.45 ± 0.12	–	−3.29 ± 0.57	−3.84 ± 0.15	−2.89 ± 0.89
E4	25.61 ± 0.18	2.48 ± 0.38	4.43 ± 0.48	1.30 ± 0.43	0.42 ± 0.08	–	−3.47 ± 0.17	−3.68 ± 0.18	−3.58 ± 0.60
E5	25.61 ± 0.08	2.31 ± 0.43	5.15 ± 0.74	1.46 ± 0.48	0.34 ± 0.08	0.88 ± 0.60	−3.54 ± 0.19	−3.60 ± 0.18	−3.80 ± 0.43
E6	25.51 ± 0.14	2.08 ± 0.23	5.10 ± 0.50	1.91 ± 0.59	0.29 ± 0.04	0.57 ± 0.22	−3.51 ± 0.10	−3.58 ± 0.14	−3.14 ± 0.57
E7	25.79 ± 0.18	4.99 ± 0.69	9.94 ± 0.94	3.60 ± 0.83	0.36 ± 0.06	1.06 ± 0.60	−3.47 ± 0.22	−3.36 ± 0.14	−3.34 ± 0.38
E8	26.07 ± 0.26	5.18 ± 0.60	17.63 ± 1.09	5.52 ± 1.24	0.22 ± 0.03	0.31 ± 0.09	−3.59 ± 0.19	−3.27 ± 0.10	−3.13 ± 0.37
E9	26.15 ± 0.15	6.47 ± 0.66	15.69 ± 0.71	5.37 ± 0.72	0.31 ± 0.03	0.65 ± 0.19	−3.35 ± 0.09	−3.64 ± 0.06	−3.56 ± 0.16
E10	25.80 ± 0.07	3.19 ± 0.35	9.61 ± 0.66	2.70 ± 0.51	0.26 ± 0.03	0.43 ± 0.13	−3.60 ± 0.16	−3.45 ± 0.10	−3.48 ± 0.20
E11	25.78 ± 0.18	3.49 ± 0.42	9.96 ± 0.49	3.92 ± 0.65	0.25 ± 0.03	0.41 ± 0.12	−3.60 ± 0.19	−3.58 ± 0.08	−3.25 ± 0.33
E12	25.56 ± 0.07	1.86 ± 0.42	6.63 ± 0.60	1.85 ± 0.51	0.22 ± 0.05	0.29 ± 0.15	−3.95 ± 0.28	−3.71 ± 0.13	−3.75 ± 0.34
E13	25.89 ± 0.06	4.49 ± 0.52	16.60 ± 0.67	5.18 ± 0.67	0.21 ± 0.03	0.26 ± 0.07	−3.93 ± 0.20	−3.61 ± 0.07	−3.63 ± 0.20
E15	25.69 ± 0.07	4.04 ± 0.34	12.52 ± 0.41	4.30 ± 0.55	0.24 ± 0.02	0.36 ± 0.08	−4.05 ± 0.15	−3.97 ± 0.05	−3.82 ± 0.20
E16	25.90 ± 0.08	4.65 ± 0.44	18.01 ± 0.45	5.54 ± 0.34	0.20 ± 0.02	0.24 ± 0.05	−4.16 ± 0.13	−4.14 ± 0.04	−4.21 ± 0.08
E17	26.19 ± 0.06	13.23 ± 0.64	45.54 ± 0.60	14.94 ± 0.45	0.22 ± 0.01	0.30 ± 0.03	−4.33 ± 0.08	−4.31 ± 0.02	−4.30 ± 0.04
E18	25.95 ± 0.11	10.45 ± 0.34	68.58 ± 0.69	23.23 ± 0.46	0.114 ± 0.004	0.06 ± 0.01	−21.85 ± 0.06	−21.64 ± 0.02	−21.66 ± 0.05
E19	25.79 ± 0.14	9.85 ± 0.32	54.79 ± 0.47	18.88 ± 0.41	0.134 ± 0.004	0.10 ± 0.01	−21.44 ± 0.09	−21.30 ± 0.02	−21.37 ± 0.06
E20	25.91 ± 0.06	9.54 ± 0.43	52.25 ± 0.52	18.05 ± 0.49	0.136 ± 0.006	0.10 ± 0.01	−20.95 ± 0.10	−20.95 ± 0.02	−20.87 ± 0.06
E21	25.83 ± 0.14	10.45 ± 0.28	43.26 ± 0.37	13.91 ± 0.30	0.183 ± 0.005	0.20 ± 0.01	−17.13 ± 0.06	−17.03 ± 0.03	−17.01 ± 0.07
E22	25.76 ± 0.13	5.30 ± 0.30	25.97 ± 0.34	9.25 ± 0.29	0.150 ± 0.009	0.13 ± 0.02	−15.51 ± 0.12	−15.54 ± 0.02	−15.47 ± 0.06
E23	≤ 25.53	2.05 ± 0.53	6.41 ± 1.29	1.76 ± 0.57	0.25 ± 0.08	0.40 ± 0.28	2.86 ± 0.47	2.61 ± 0.36	2.79 ± 0.54

Notes. [a] Using the equations from Decock et al. (2013) and error propagation, the first 4 rows are omitted as they are closer to the asymptotic value.